Monte Carlo functional estimation of the radiative source term in a semi–transparent medium: A faster coupled conductive–radiative model resolution

Léa Penazzi, Olivier Farges, Yves Jannot, Johann Meulemans, Vincent Schick

Monte Carlo functional estimation of the radiative source term in a semi-transparent medium: a faster coupled conductive–radiative model resolution

Léa Penazzi[a,b], Olivier Farges[a,b], Yves Jannot[a,b], Johann Meulemans[b,c] and Vincent Schick[a,b]

[a] Université de Lorraine, CNRS, LEMTA, Vandœuvre-lès-Nancy, F–54500, France
[b] Laboratoire Commun Canopée, CNRS, Université de Lorraine, Saint–Gobain,
[c] Saint–Gobain Research Paris, 39 quai Lucien Lefranc, Aubervilliers, F–93303, France

ARTICLE INFO

Keywords:
Semi-transparent medium
Conduction
Radiation
Transfer function
Monte Carlo method

ABSTRACT

The estimation of thermo-physical properties of materials at high temperatures requires the development of robust and fast-enough direct models that takes into account the strong coupling between conduction and radiation. The interest in using the Monte Carlo method to obtain a conduction–radiation model in a semi-transparent material solved in a reduced computational time is addressed in this study. An academic configuration that consists of an absorbing/emitting and non-scattering gray medium with steady-state conduction is investigated since this study is meant to be a proof of concept. It is demonstrated that the radiative source term of the heat equation may be estimated as a function of the temperature field to the fourth power, using a Finite Differences algorithm and a single Monte Carlo simulation of radiation. The results of the numerical study show that, on the one hand, they are in good agreement with those found in the literature and, on the other, that the coupled model can be resolved in a significantly shorter amount of computational time than with traditional methods thanks to the functional estimation of the radiative source term. In fact, in each of the fifteen analyzed cases, the coefficients of the function were determined in approximately 6s using the Monte Carlo method using a laptop with standard computational resources. The computation of the function and its application revealed that, depending on the studied configuration, a resolution with the finite differences–functional Monte Carlo algorithm can be around twenty to one thousand times faster than a classic Finite Differences–Monte Carlo algorithm. Due to these characteristics, as well as the fact that the functional estimation is insensitive to the associated geometry's complexity and can be extended to configurations with heterogeneous radiative properties, it becomes possible to utilize this method in inversion procedures, since the direct model must be evaluated numerous times.

1. Introduction

Reducing the carbon footprint of high-temperature manufacturing processes (e.g., glass furnaces) is one of the industry's most pressing current concerns [50]. At the considered temperatures (beyond 1000 °C), measurements and instrumentation are challenging. Because of this, the behavior of materials involved in these processes is not always accurately modeled. In this context and in order to limit heat losses, it is necessary to optimize the usage of materials in these processes [28]. To attain this objective, it is essential to develop methods for measuring the thermophysical properties of these materials at their operating temperature.

The estimation methodology for thermophysical properties of materials is founded on a triad of experimental measurements, a direct model and inversion algorithm [19]. Since the estimation of thermal properties is highly dependent on the model involved, one of the greatest challenges is to develop direct models that account for the significant conduction–radiation coupling in the sample at high temperature [37]. As a matter of fact, the insulating materials employed in such applications are often refractory ceramic foams composed of silica and/or alumina that have a heterogeneous and complex structure [24, 25]. These materials are semi-transparent to radiation at high temperatures, meaning that emitting/absorbing and scattering processes occur within the volume. Thus, both the conduction-radiation coupled heat transfer and the possibly complex geometry of the experimental setup and the sample must be considered. In addition, for this coupled model to be employed in an estimation methodology, it must provide a reasonable trade-off between accuracy and speed of execution for the model's resolution.

In the majority of inverse processes associated with the estimation of thermal properties at high temperatures (thermal conductivity or diffusivity, for example), either purely conductive models or coupled models with assumptions on the optical properties (no scattering events, grey medium etc.) have been used [20, 21]. Thus, a robust coupled direct model is required in which these assumptions can be eliminated and which is not restricted to an asymptotic approach (optically thick or thin media). Prior research established the viability and use of the Monte Carlo method for solving coupled and transient thermal problems in the context of characterizing complex media [41].

The development and resolution of a coupled conduction–radiation model in a semi-transparent medium are addressed in the current work. A methodological choice has been taken

*Corresponding author
leapenazzi@gmail.com (L. Penazzi)
ORCID(s): 0000-0002-0377-6192 (L. Penazzi)

to concentrate on three semi-analytical solutions developed by Viskanta et al.. The first case's solution (1) corresponds to a pure absorbing medium with black walls [46], the second (2) to a pure absorbing medium with grey walls [45], and the third to an absorbing and scattering medium with black walls [44]. Viskanta et al. derived the solution of these cases by reducing a nonlinear integro-differential equation to a nonlinear integral equation dependent on exponential integral functions. The numerical results were derived via an iterative process. As, to the best of the authors' knowledge, relatively few analytical solutions exist in the literature relating coupled conduction-radiation problems in semi-transparent media [15], these reference examples have been extensively studied. The first case (1) was studied by Asllanaj et al. [1] utilizing the Finite Volume Method (FVM) to solve the radiative source term based on a cell vertex scheme and associated to a modified exponential scheme. The heat transfer equation was solved using finite elements of low or high order. Perraudin & Haussener [38] investigated this problem (1) by quantifying the coupling effects in a macro-porous medium by solving the volume-averaged continuum equations with effective transport equations. They developed a computational method employing cell-centered finite volumes and Monte Carlo ray tracing methods to solve coupled heat transfer using a structured mesh. Ouchtout et al. [32] recently proposed a Finite Element Method (FEM) framework to describe the coupled heat transfer inside a heterogeneous medium at discrete and continuous scales and they compared their methods on cases (1) and (3).

In this study, the transient heat transfer equation is solved using the Finite Differences Method (FDM), and the volumetric radiation is solved using the Monte Carlo Method (MCM). The novelty and interest of this method lay in the functional estimation of the radiative source term with the MCM, which enables the evaluation of the temperature field in a significantly shorter amount of time than traditional methods. This functional estimation is performed with a single Monte Carlo computation without compromising the complexity of either the physics or the geometry, as no intersections of the rays with the mesh are needed. This function can therefore be directly used at each iteration of the FDM algorithm, resulting in a significant reduction in computational time in comparison to a standard direct model resolution in which the MCM computation is performed at each iteration. The estimation of a function of physical quantities with the MCM was initially referred to as *Inverse Monte Carlo* and *Symbolic Monte Carlo* in the field of radiative transfer [6, 7, 13, 27] and has only recently been applied to coupled heat transfer [35, 34, 33].

From analytical to complex geometries, in radiative transfer problems resolution, the estimation of a physical quantity as a transfer function depending linearly on source parameters is a common practice. In the case of transparent media and surface-to-surface radiative heat exchanges, the computation of view factors is essential [30]. In practice, when the number of surfaces is large and the geometries are complex, these computations can be costly, and numerous methods attempt to pre-calculate these view factors to reduce computation time and complexity. Monte Carlo methods are commonly employed in standard practice to calculate view factors, particularly when estimating net flux exchanged. In such cases, view factors can be calculated once and for all with a single Monte Carlo calculation [8, 31]. This practice is inspired by analytical view factors calculations from the work of [14, 17, 18, 30]. Even though the current study's methodology does not follow the same path, it reaches the same conclusion. In contrast, the view factors (i.e., the coefficients of this linear function) are explicit in the practice described here, whereas they are implicit in the practice described previously. In other words, the concept of a radiative quantity as a linear transfer function with respect to sources is inherent to the Monte Carlo practice in radiative transfer, particularly in transparent media.

Several research groups have calculated the components of the linear operator expressing the radiative source term as a function of the temperature field to the fourth power for a gray semi-transparent medium in the case of participating media in which radiative exchanges occur in volume. The functional estimation of the radiative source term presented in this article is conceptually comparable to the Monte Carlo Ray-Tracing technique based on radiative exchange factors. [40, 23, 42]. This method was first described at the start of this century, and before it, K. Kudo developed a similar technique known as *Radiant Energy Absorption Distribution* (READ) [47] in the 1990s. More recently, Li et al. [22] extended this Monte Carlo method based on the READ concept to problems involving combined conduction-radiation heat transfer in irregular geometries with cartesian grids. In addition, Zarrouati et al. [48] applied this method to absorbing/emitting and scattering medium in which a matrix of probabilities $\mathcal{P}^{ea}_{IJ}$ is introduced, where an element $\mathcal{P}^{ea}_{ij}$ of the matrix is the probability that a ray emitted by a cell i is absorbed by a cell j. $\mathcal{P}^{ea}_{IJ}$ is evaluated by a classical Monte Carlo ray tracing technique and independent of the temperature field. Consequently, the vector of the radiative powers deposited within the cells has a very straightforward expression, as it is a linear operator of the vector T^4, with the components of this linear operator (i.e., the matrix) being expressly related to the probabilities matrix. Similar to the current study, Zarrouati et al. worked on absorbing/emitting and scattering media in the case of black walls. When the results are presented, the coefficient matrices of the functions will be specified for the purpose of analysis. Unlike the radiative exchange factors method, the functional Monte Carlo method presented here does not require meshing the volume and dividing it into sub-volumes or surface elements in order to estimate the radiative source term for the heat conduction equation.

In other regards and due to the advantages of fast calculation, the P_1 approximation has been used to estimate the radiative source term in potentially non-gray participating media problems associated with engineering research involving conjugated heat transfer [2] or thermal transfer

coupled to chemical reaction kinetics [3, 4] for instance. This method was also applied in a numerical study on the influence of radiative heat transfer on parallel hot-wire thermal conductivity measurements at high temperature [37], showing the limitations of the the P_1 approximation and the need for the development of a coupled conduction-radiation model free from the diffusion approximation.

The goal of this study is to provide a proof-of-concept of the procedure in an academic case that can be expanded in the future to more complicated cases. In light of this, the reader may be aware that the entire algorithm is designed for a general case in which radiative properties depend on frequency, despite the fact that the method is implemented in grey media cases in the Results section and that the current investigation is restricted to non-temperature dependent thermophysical properties. The heat transfer model of the academic configuration is described first in Sec. 2.1, followed by the algorithm of resolution, which consists of a *classic* resolution with the MCM (see Sec. 2.4) and a *functional* estimation of the radiative source term with the MCM coupled with the FDM resolution (see Sec. 2.5). The results are then compared to semi-analytical solutions from [46, 45, 44], which serve as a benchmark in Sec. 3.1, Sec. 3.2 and Sec. 3.3. After this, the benefits of adopting the functional estimate MC-FD approach in terms of calculation time are demonstrated in Sec. 3.4. Finally, conclusions and perspectives for the future research studies are offered Sec. 5.

2. Models and methods

2.1. Studied configuration

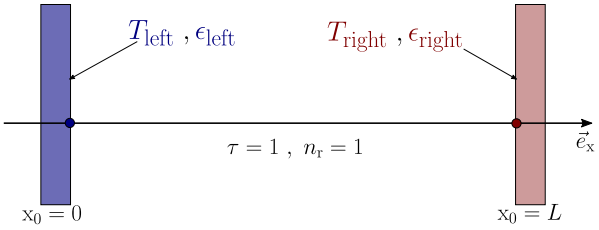

Figure 1: Schematic view the configuration assimilated to a hot plate configuration.

The studied configuration is represented on Fig. 1 and corresponds to the three cases developed in Viskanta et al. references [46, 45, 44]. The system is comprised of a gray, absorbing/emitting and scattering medium $\mathcal{D}$ bounded by two diffuse, non black, infinite, isothermal and parallel plates ($\partial\mathcal{D} \equiv \partial\mathcal{D}_{\text{left}} \cup \partial\mathcal{D}_{\text{right}}$). The problem can be considered one-dimensional, along the axis $O\vec{e}_{\text{x}}$. The plate has a unit length of $L = 1$ m and the optical thickness τ is set equal to 1. The plates temperatures set at T_{left} and T_{right} are respectively located in $(\vec{\text{x}} = 0, 0, 0)$ and $(\vec{\text{x}} = L, 0, 0)$ with emissivities ϵ_{left} and $\epsilon_{\text{right}} \leq 1$. In this problem, conduction is at steady-state and radiation within the volume $\mathcal{D}$. The equations describing the system are the following :

$$\begin{cases} \lambda\Delta T - \vec{\nabla}\cdot\vec{q}_{\text{R}} = 0 & \forall \vec{x} \in \mathcal{D} \quad (1) \\ T(\text{x}_0 = 0) = T_{\text{left}} & \forall \vec{x} \equiv \vec{y} \in \partial\mathcal{D}_{\text{left}} \quad (2) \\ T(\text{x}_0 = L) = T_{\text{right}} & \forall \vec{x} \equiv \vec{y} \in \partial\mathcal{D}_{\text{right}} \quad (3) \end{cases}$$

The radiative source term $-\vec{\nabla}\cdot\vec{q}_{\text{R}}$ from Eq. (1) may be obtained from a radiative balance of a homogeneous and isothermal volume $\mathcal{V}$ expressed as follows:

$$\begin{aligned} \Phi_{\mathcal{V}} &= \int_{\mathcal{V}} \left(-\vec{\nabla}\cdot\vec{q}_{\text{R}}\right) d\mathcal{V} \\ &= \int_{\mathcal{V}} d\mathcal{V} \int_{4\pi} d\vec{\omega} \int_0^{+\infty} d\nu\, k_{\text{a},\nu} \left(\mathcal{I}_\nu^{\text{eq}}(\vec{x}) - \mathcal{I}_\nu(\vec{x},\vec{\omega})\right) \end{aligned} \quad (4)$$

In Eq. (4), $d\mathcal{V}$ corresponds to an elementary volume element, $d\vec{\omega}$, to the solid angle, $k_{\text{a},\nu}$ to the spectral absorption coefficient and ν to the frequency. In the present study, homogeneous spectral radiative properties are considered. The blackbody spectral intensity $\mathcal{I}_\nu^{\text{eq}}$ is expressed with the Planck's law.

$$\mathcal{I}_\nu^{\text{eq}}(\vec{x}) = \frac{2h\nu^3}{c^2} \frac{1}{e^{\frac{h\nu}{k_{\text{B}}T(\vec{x})}} - 1} \quad (5)$$

With h the Planck constant (in $\text{kg}\,\text{m}^2\,\text{s}^{-1}$), $c = c_0/n$, the speed of light in the medium (in $\text{m}\,\text{s}^{-1}$) with c_0 the speed of light in the vacuum and n, the refractive index in the semi-transparent medium, k_{B}, the Boltzmann constant (in $\text{J}\,\text{K}^{-1}$) and $T(\vec{x})$ the temperature at the $\vec{x}$ location. $\mathcal{I}_\nu(\vec{x},\vec{\omega})$ is the spectral radiative intensity (in $\text{W}\,\text{m}^{-2}\,\text{sr}^{-1}\,\text{cm}^{-1}$) at the location $\vec{x}$ in direction $\vec{\omega}$ and is solution of the following Radiative Transfer Equation (RTE) [30]:

$$\begin{aligned} \vec{\omega}.\vec{\nabla}\mathcal{I}_\nu(\vec{x},\vec{\omega}) = &-(k_{\text{a},\nu} + k_{\text{s},\nu})\mathcal{I}_\nu(\vec{x},\vec{\omega}) + k_{\text{a},\nu}\mathcal{I}_\nu^{\text{eq}} \\ &+ k_{\text{s},\nu} \int_{4\pi} \text{P}_{\text{sca},\nu}(\vec{x},\vec{\omega}|\vec{\omega}')\mathcal{I}_\nu(\vec{x},\vec{\omega}')d\vec{\omega}' \end{aligned} \quad (6)$$

Where $\vec{\omega}$ is the unit direction, k_{s}^ν, the spectral scattering coefficient and $\text{P}_{\text{sca},\nu}$, the scattering phase function.

In this study the heat equation corresponding to Eq. (1) is solved with the FDM (see Sec. 2.2) and the radiative source term is solved with the Monte Carlo method (see Sec. 2.3), implying no linearization of the radiative source term. The complete finite differences and Monte Carlo algorithm is presented in Sec. 2.4.

2.2. Heat conduction numerical resolution

The laplacian term ΔT of the Eq. (1) is approximated using a second–order centered finite differences scheme in such a way that:

$$\Delta T = \frac{T[i+1] - 2T[i] + T[i-1]}{\delta_{\text{x}}^2} \quad (7)$$

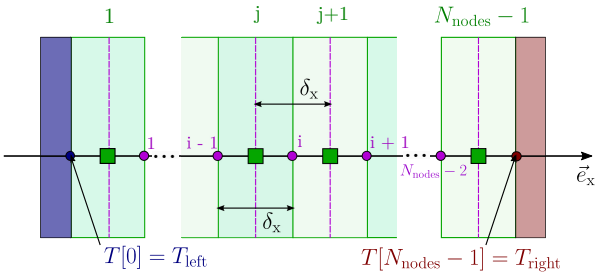

Figure 2: Schematic view the 1D configuration in which conductive nodes are represented with purple circles and radiative nodes, with green squares.

The 1D bar is discretized into a number N_{nodes} of meshes and the spatial step is identified as δ_x. The conduction meshes are indexed by the index i ranging from 0 to $N_{\text{nodes}} - 1$, as represented using purple circles on Fig. 2. Each node i is located at the center of a conductive mesh, each mesh has a width δ_x and in the FDM the assumption made is that the temperature of each conductive mesh is homogeneous. By inserting Eq. (7) into Eq. (1), one obtains the following equation:

$$T[i] = \frac{1}{2}\left(T[i+1] + T[i-1]\right) - \frac{\delta_x^2}{2\lambda} S_{\text{ray}}[i] \tag{8}$$

The previous equation is valid for $i \in \{1 : N_{\text{nodes}} - 2\}$. For the two boundary nodes, in $i = 0$ and $i = N_{\text{nodes}} - 1$, the temperature values are set and respectively equal to T_{left} and T_{right}.

The volumetric radiative source term S_{ray} in $\mathrm{W\,m^{-3}}$ is calculated at each iteration of the finite differences algorithm for each conductive node i. To this end, the radiative source term $\Phi_{\mathcal{L}}$[1] is estimated for each radiative node j with a Monte Carlo computation and then equally allocated between the two conductive nodes nearby, such as :

$$S_{\text{ray}}[i] = \frac{\Phi_{\mathcal{L}}[j] + \Phi_{\mathcal{L}}[j-1]}{2\delta_x} \tag{9}$$

The radiative mesh is chosen slightly shifted from the conductive mesh and in each radiative mesh, the radiative source term $\Phi_{\mathcal{L}}$ is homogeneous. In Fig. 2, the radiative meshes, represented in green squares, are stated with the index j ranging from 0 to N_{nodes}. Taking into account the left wall contribution, with a mesh element referenced at $j = 0$ and the right wall contribution in $j = N_{\text{nodes}}$, there is a total of $N_{\text{nodes}} + 1$ radiative meshes ($N_{\text{nodes}} - 1$ meshes added to the two walls contributions).

2.3. Estimation of the radiative source term with the MCM

In each node j of the radiative mesh, the radiative source term $\Phi_{\mathcal{L}}$ is estimated with a Monte Carlo computation. In order to estimate the source term with a Monte Carlo algorithm, Eq. (4) must be translated into statistical terms.

The solid angle $d\vec{\omega}$ may be expressed as follows :

$$\int_{4\pi} d\vec{\omega} = \int_{2\pi} d\varphi \int_0^{\pi} \sin(\theta) d\theta \tag{10}$$

Given the polar and azimuthal angles, respectively θ and φ, injecting Eq. (10) in Eq. (4) gives:

$$\begin{aligned} &\Phi_{\mathcal{L}} = \\ &\int_D p_X(\vec{x})\, d\vec{x} \int_{2\pi} p_\Phi(\varphi)\, d\varphi \int_0^{\pi} p_\Theta(\theta)\, d\theta \ \cdots \\ &\cdots \int_{\nu_{\min}}^{\nu_{\max}} p_N(\nu) d\nu \, \frac{k_{a,\nu}\left(\mathcal{I}_\nu^{\text{eq}} - \mathcal{I}_\nu(\vec{x},\vec{\omega})\right)}{p_X(\vec{x})\, p_\Phi(\varphi)\, p_\Theta(\theta)\, d\theta\, p_N(\nu)} \\ &\Leftrightarrow \Phi_{\mathcal{L}} = \mathbb{E}\underbrace{\left(\frac{k_{a,\nu}\left(\mathcal{I}_\nu^{\text{eq}} - \mathcal{I}_\nu(\vec{x},\vec{\omega})\right)}{p_X(\vec{x})\, p_\Phi(\varphi)\, p_\Theta(\theta)\, p_N(\nu)}\right)}_{W} \end{aligned} \tag{11}$$

By incorporating probability density functions, the previous equation can be given a statistical interpretation. In fact, the integral expression of the radiative source term of Eq. (11) can be read as the expectation of a random variable W, the Monte Carlo weight, such as $\Phi_{\mathcal{L}} = \mathbb{E}(W)$. Then each of the following elements can be identified :

- Sampling of an emission location $\vec{x}$ within the medium : $p_X(\vec{x}) = \frac{1}{\delta_x}$ is the uniform probability density related to the distribution of a photon emission location $\vec{x}$ between $(x_0 = 0, 0, 0)$ and $(x_0 = L, 0, 0)$, in which $\vec{X}$ is defined as the random variable related to the location within the medium D and $\vec{x}$ its realization.
- Sampling of an emission direction $\vec{\omega}$: The emission direction is calculated with the successive sampling of the polar angle θ and azimuthal angle φ. In the case of an isotropic emission, each of the probability densities are based on the definition of the solid angle from Eq. (10). The polar angle random variable Θ is sampled uniformly between 0 and π with the related probability density $p_\Theta(\theta) = \frac{\sin(\theta)}{2}$ and its realization is denoted θ. The azimutal angle random variable Φ is sampled uniformly between 0 and 2π with the related probability density $p_\Phi(\varphi) = \frac{1}{2\pi}$ and its realization is denoted φ (see Fig. 3). The ratio $1/4\pi$ is the result of the solid angle integration over the sphere 4π
- Sampling of a frequency ν : A frequency ν is sampled according to the probability density function $p_N(\nu)$ within the interval $[\nu_{\min}; \nu_{\max}]$, then the monochromatic absorption coefficient $k_{a,\nu}$ can be calculated as well as the black body spectral intensity $\mathcal{I}_\nu^{\text{eq}}$ and the spectral radiative intensity $\mathcal{I}_\nu(\vec{x},\vec{\omega})$.

[1] The heat flux $\Phi_{\mathcal{V}}$ in W estimated in Eq. (4) is integrated over the length $\mathcal{L}$ and becomes a surfacic heat flux is expressed as $\Phi_{\mathcal{L}} = \int_{\mathcal{L}} (-\vec{\nabla} \cdot \vec{q}_R)\, dl = \int_{\mathcal{L}} dl \int_{4\pi} d\vec{\omega} \int_0^{+\infty} d\nu k_{a,\nu} \left(\mathcal{I}_\nu^{\text{eq}}(\vec{x}) - \mathcal{I}_\nu(\vec{x},\vec{\omega})\right)$ in $\mathrm{W\,m^{-2}}$.

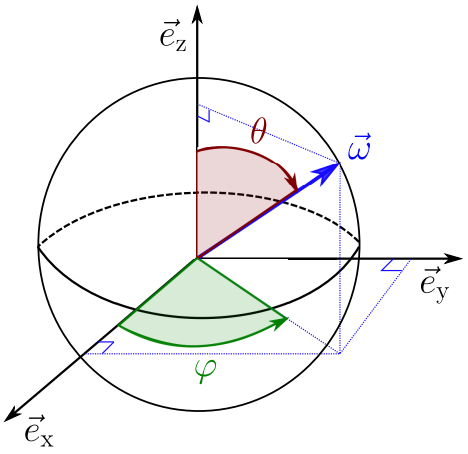

Figure 3: Definition domains of the polar angle θ and azimuthal angle φ.

- The Monte Carlo weight w : At the end of each k$^{\text{th}}$ realization of the algorithm, the value of w_k corresponding to a realization of the Monte Carlo weight random variable W is saved. In Eq. (11), however, if $\mathcal{I}_\nu^{eq}$ can be calculated from Eq. (5), the value of the spectral radiative intensity $\mathcal{I}_\nu(\vec{x},\vec{\omega})$ remains unknown. This value can be determined using the reverse Monte Carlo algorithm, as described in Appendix A. Optical paths are sampled until an emission location $\vec{X}_{end}$ is encountered and the path ceases; eventually, the Monte Carlo weight can be estimated and stored (see Eq. (14)).

A Monte Carlo computation consists in sampling N_{MC} optical paths, providing N_{MC} optical paths, providing N_{MC} realizations $w_1, w_2, ..., w_{N_{MC}}$ of W, and then estimate the radiative source term $\Phi_{\mathcal{L}}$ as the mean value m of these Monte Carlo weights realizations. The estimation m of the source term and the estimation s of the uncertainty associated are detailed in the following equations :

$$\begin{cases} \Phi_{\mathcal{L}} \approx m = \dfrac{1}{N_{MC}} \displaystyle\sum_{k=1}^{N_{MC}} w_k & (12) \\ s = \dfrac{1}{\sqrt{N_{MC}}} \left(\dfrac{1}{N_{MC}} \displaystyle\sum_{k=1}^{N_{MC}} w_k^2 - m^2 \right)^{\frac{1}{2}} & (13) \\ w_k = \dfrac{\delta_x \, 4\pi \, k_{a,\nu} \left(\mathcal{I}_\nu^{eq}[j_{start}] - \mathcal{I}_\nu^{eq}[j_{end}] \right)}{p_N(\nu)} & (14) \end{cases}$$

One estimation m is performed for each mesh element $j \equiv j_{start}$ of the radiative mesh. Hence, at each iteration of the finite difference algorithm, $N_{nodes} - 1$ Monte Carlo computations are carried out.

From Eq. (11), the essence of the path sampling for one realization of w_k may be derived and is represented in Fig. 4, the latter runs as follows :

0 A starting position $\vec{x}_{start}$ is sampled uniformly within the wall of thickness L (between $x = 0$ and $x = L$) according to the probability density $p_X(\vec{x})$.

1 The current position $\vec{x}_c$ value is set equal to $\vec{x}_{start}$. Then, a direction $\vec{\omega}$ is sampled with the successive samplings of the angles φ and θ according to the probability densities $p_\Phi(\varphi)$ and $p_\Theta(\theta)$. A frequency ν is sampled between ν_{min} and ν_{max} according to $p_N(\nu)$. An extinction length l is sampled according to the exponential Beer-Lambert law (depending on the extinction coefficient $\beta_\nu = k_{a,\nu} + k_{s,\nu}$) and the current position $\vec{x}_c$ value is actualized to $\vec{x}_c + l\vec{\omega}$.

2 A test is performed to identify if the current position $\vec{x}_c$ is still within the volume $\mathcal{D}$ or at the medium boundary $\partial\mathcal{D}$ (either $\partial\mathcal{D}_{left}$ in or $\partial\mathcal{D}_{right}$).

3 If $\vec{x}_c \in \mathcal{D}$, a random variable r is sampled according to a uniform law between 0 and 1. r value is compared to the scattering albedo $\frac{k_s^\nu}{\beta^\nu}$, corresponding to a probability :

- If $r < \frac{k_s^\nu}{\beta^\nu}$, a scattering event occurred in $\vec{x}_c$ and the algorithm carries on with step 1.
- Else, an absorption event occurred in $\vec{x}_c$, path stops and the Monte Carlo weight is stored.

3 If $\vec{x}_c \in \partial\mathcal{D}$, a test is performed to identify which of the two boundary was reached :

- If $\vec{x}_c \in \partial\mathcal{D}_{left}$ ($\vec{x}_c \equiv \vec{y}_{left}$), a random variable r is sampled uniformly between 0 and 1 and compared to the value of the wall emissivity ϵ_{left} (step 4$_a$). If $r < \epsilon_{left}$ (homogeneous to a probability), absorption occurs on the left wall, the path stops and the Monte Carlo weight is stored. Else, $r > \epsilon_{left}$: a reflection event occurs (step 5$_a$), a direction $\vec{\omega}$ is sampled uniformly on the hemisphere and the current position is set to $\vec{y}_{left} + ||\vec{y}_{left} - \vec{x}_c||\vec{\omega}$.
- If $\vec{x}_c \in \partial\mathcal{D}_{right}$ ($\vec{x}_c \equiv \vec{y}_{right}$), similarly to the previous described steps either an absorption event occurs on the right wall (step 4$_b$, $r < \epsilon_{right}$) and path stops, or a reflection event occurs (step 5$_b$) and the path goes on in the medium at a position $\vec{y}_{right} + ||\vec{x}_c - (\vec{y}_{right} - \vec{y}_{left})||\vec{\omega}$.

6 After reflection events on both boundaries, a uniform random variable r is sampled and, similarly to step 3, compared to the scattering albedo probability $\frac{k_{s,\nu}}{\beta_\nu}$. Either an absorption event occurs in $\vec{x}_c$ and the path stops, or a scattering event occurs and the path goes on in the medium (see step 1).

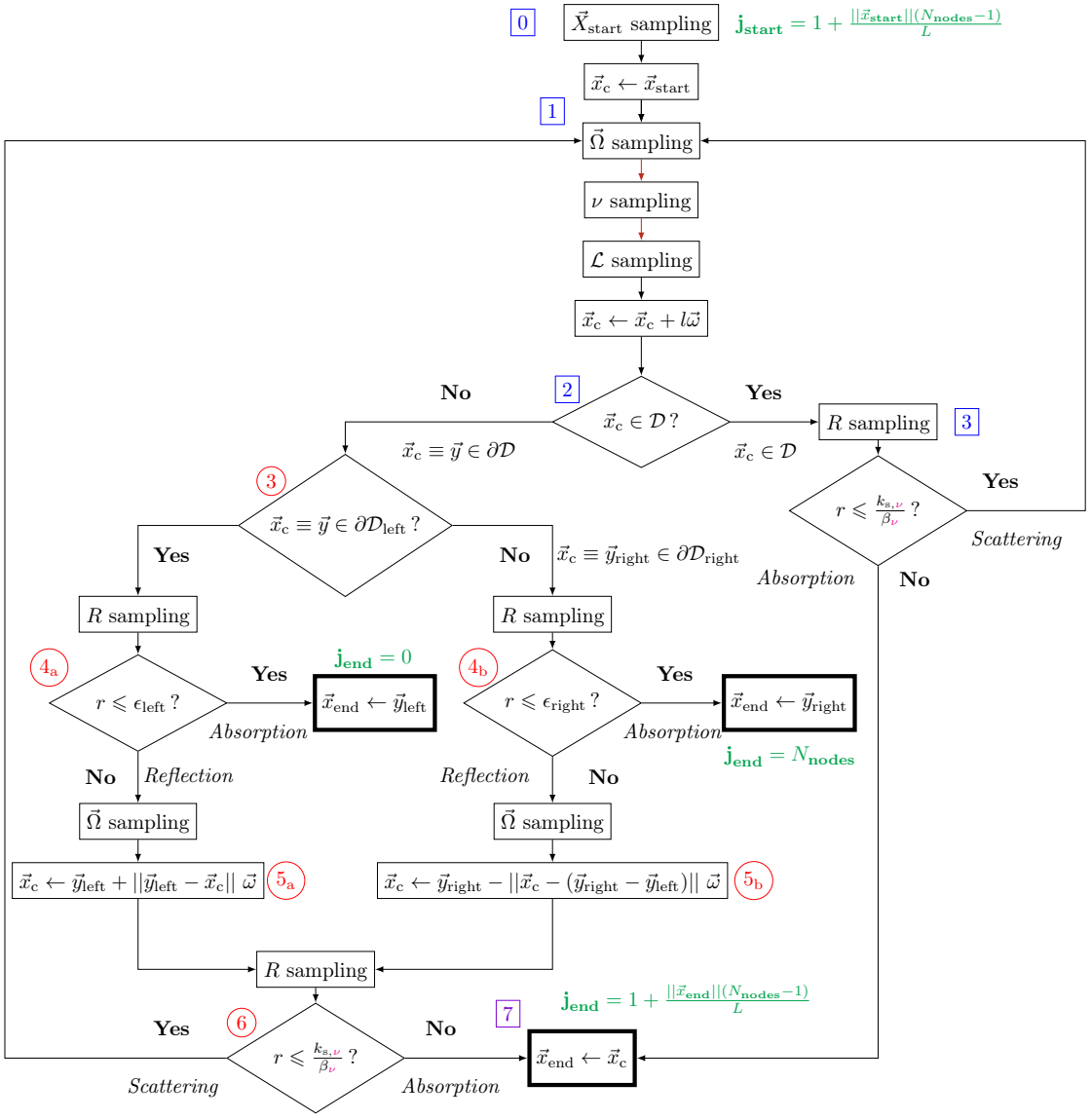

Figure 4: Path sampling algorithm corresponding to one realization of the Monte Carlo algorithm to estimate $\Phi_{\mathcal{L}}$.

In summary, the path starts at a location $\vec{x}_{\text{start}}$ in the medium in the mesh indexed $\mathrm{j}_{\text{start}} = 1 + \frac{||\vec{x}_{\text{start}}||(N_{\text{nodes}}-1)}{L}$ and this path can either end at one of the two boundaries or within the medium :

- If the path ends in $\partial\mathcal{D}_{\text{left}}$, $\vec{x}_{\text{end}} \equiv \vec{y}_{\text{left}}$ and the corresponding radiative mesh index is $\mathrm{j}_{\text{end}} = 0$.
- If the path ends in $\partial\mathcal{D}_{\text{right}}$, $\vec{x}_{\text{end}} \equiv \vec{y}_{\text{right}}$ and the corresponding radiative mesh index is $\mathrm{j}_{\text{end}} = N_{\text{nodes}}$.
- If the path ends in the medium $\mathcal{D}$, the corresponding radiative mesh index is retrieved and stored $\mathrm{j}_{\text{end}} = 1 + \frac{||\vec{x}_{\text{end}}||(N_{\text{nodes}}-1)}{L}$.

At the end of each k^{th} path, the corresponding Monte Carlo weight is stored such as described in Eq. (14). For illustration purposes, Appendix B contains two examples of potential optical paths sampled with the Monte Carlo algorithm to estimate the radiative source term.

2.4. Finite differences and Monte Carlo algorithm

The finite differences algorithm operates with two temperature vectors. The first one, $\vec{T}_{\text{new}}$ gathers all the N_{nodes} values of temperatures, at each node, at the n^{th} iteration of the finite differences algorithm. The second one, $\vec{T}_{\text{old}}$ gathers all the N_{nodes} values of temperatures at the previous $(n-1)^{\text{th}}$ iteration.

As described in the Algorithm 2.1, the $\vec{T}_{\text{old}}$ vector is firstly initialized with its values set equal to $\vec{T}_{\text{new}}$. Then, for each radiative mesh element j, a Monte Carlo computation is performed to estimate each source term $\Phi_{\mathcal{L}}[j]$. Afterward, for each conductive node i the radiative source term $S_{\text{ray}}[i]$ is computed. Eventually the corresponding $\vec{T}_{\text{new}}$ profile at the

Algorithm 2.1: Computation of the temperature profile $\vec{T}_{\text{new}}$ with the finite differences and Monte Carlo algorithms.

while $\varepsilon >$ tolerance **do**
  $\vec{T}_{\text{old}} \leftarrow \vec{T}_{\text{new}}$ *%Initialization*
  for $j = 1 : N_{\text{nodes}} - 1$ **do**
    Monte Carlo estimation of $\Phi_{\mathcal{L}}[j]$
  end
  for $i = 0 : N_{\text{nodes}} - 1$ **do**
    for $j = 1 : N_{\text{nodes}} - 1$ **do**
      Calculation of $S_{\text{ray}}[i]$ (see Eq. (9))
    end
    Calculation of each $\vec{T}_{\text{new}}[i]$ (see Eq. (8))
    $\varepsilon \mathrel{+}= \frac{||\vec{T}_{\text{new}}[i] - \vec{T}_{\text{old}}[i]||}{\vec{T}_{\text{new}}[i]}$
  end
end

n^{th} iteration of the finite differences algorithm can be computed and the tolerance criterion ε can be estimated. Given an arbitrary value of the tolerance criterion, the previous finite differences algorithm carries on until the computed ε value is lower than the tolerance criterion.

2.5. The corresponding functional estimation of the radiative source term with MCM

Under the assumption of a gray medium, the frequency-dependent General RTE from Eq. (6) is integrated over all frequencies of the spectral interval considered, yielding a formulation known as the Total RTE depending on a total radiative intensity $\mathcal{I}(\vec{x}, \vec{\omega})$. When the blackbody spectral intensity derived from Eq. (5) is integrated over the entire frequency domain and the refractive index n is set to 1, the blackbody intensity can be expressed as follows:

$$\mathcal{I}^{\text{eq}} = \frac{\sigma_{\text{SB}}}{\pi} T^4(\vec{x}) \tag{15}$$

With σ_{SB} the Stefan-Boltzmann constant.

Under these considerations, at each iteration of the finite differences algorithm, $N_{\text{nodes}} - 1$ source terms are computed with for each a Monte Carlo computation with N_{MC} optical paths sampled. These operations are time consuming and may be questioned when one notices that at each iteration of the finite differences algorithm, only one set of values change and come in input into the MC algorithm : the list of temperature at each node to the power 4 (see Fig. 5).

Given that only the value of the temperatures list $\vec{T}^4_{\text{old}}$ is modified at each iteration of the finite differences algorithm, the following methodology demonstrates how to estimate each of the $N_{\text{nodes}} - 1$ radiative source term as a function of these temperatures using a single Monte Carlo computation and what information must be stored at each path sampling. Before beginning the finite differences algorithm, $N_{\text{nodes}} - 1$ Monte Carlo computations are performed only once to estimate each $\Phi_{\mathcal{L}}[j] \equiv \Phi_{\mathcal{L}}[\text{j}_{\text{start}}]$ as a function of the temperature list at each conductive node to the fourth power:

$$\Phi_{\mathcal{L}}[\text{j}_{\text{start}}] = \text{f}\underbrace{\left(T_0^4; T_1^4; ...; T^4_{N_{\text{nodes}}-1}\right)}_{\vec{T}^4_{\text{old}}} \tag{16}$$

Let us start expressing the source term of the j^{nth} radiative element by developing Eq. (12) with the expression of the Monte Carlo weight w_{k} from Eq. (14):

$$\Phi_{\mathcal{L}}[\text{j}_{\text{start}}] \approx \frac{1}{N_{\text{MC}}} \sum_{k=1}^{N_{\text{MC}}} 4\pi k_{\text{a}} \delta_{\text{x}} \left(\mathcal{I}^{\text{eq}}[\text{j}_{\text{start}}] - \mathcal{I}[j_{\text{end},k}]\right) \tag{17}$$

In the previous equation, $\mathcal{I}^{\text{eq}}[\text{j}_{\text{start}}]$ is expressed as described by Eq. (15) regarding the temperature $T[\text{j}_{\text{start}}]$ of the radiative mesh j_{start}. $\mathcal{I}[j_{\text{end},k}] \equiv \mathcal{I}(\vec{x}, \vec{\omega})$ is the solution of the Total RTE (corresponding to Eq. (6) integrated over the whole frequency domain) for the k^{th} path. As the path undergoes successive scattering and reflection events, it always ends with an absorption event in one of the $j \equiv \text{j}_{\text{end}}$ element of the mesh, with $\text{j}_{\text{end}} \in \{0, 1, ..., N_{\text{nodes}}\}$ [2]. Hence, similarly to $\mathcal{I}^{\text{eq}}[\text{j}_{\text{start}}]$, the blackbody radiant intensity absorbed at the node j_{end} may be expressed as in Eq. (15), such as: $\mathcal{I}[j_{\text{end},k}] = \frac{\sigma_{\text{SB}}}{\pi} T^4[j_{\text{end},k}]$. Given the previous developments of each radiant intensity, the sum in Eq. (17) can be distributed and the previous expression becomes :

$$\Phi_{\mathcal{L}}[\text{j}_{\text{start}}] \approx 4k_{\text{a}}\sigma_{\text{SB}}\delta_{\text{x}}(T^4[\text{j}_{\text{start}}] - \underbrace{\frac{1}{N_{\text{MC}}} \sum_{k=1}^{N_{\text{MC}}} T^4[j_{\text{end},k}]}_{\star}) \tag{18}$$

With Eq. (18), if the aim is to estimate $\Phi_{\mathcal{L}}[\text{j}_{\text{start}}]$, a possibility could be to store at each realization k of the Monte Carlo calculation the temperature $T^4[j_{\text{end},k}]$ of each k^{th} path absorbed in the radiative mesh element $j_{\text{end},k}$. Doing so would still mean storing a temperature value of $\vec{T}_{\text{old}}$ during the Monte Carlo computation and hence, prevent the estimation of the radiative source term as a function of $\vec{T}^4_{\text{old}}$, as the temperature value would remain set. Instead of storing at each realization $T^4[j_{\text{end},k}]$, an other possibility is then to only store the radiative mesh index $j_{\text{end},k}$. In this way, the only information stored for each path will be the absorption location index $j_{\text{end},k}$ and the temperature at this end can be then computed in a post-treatment phase with the Eq. (5).

Given the previous path example detailed in Sec. 2.3 within Figs. 14 and 15, the information stored in this functional Monte Carlo algorithm would be as detailed in Fig. 6. Only one list of $(N_{\text{nodes}} + 1)$ m_j counters is necessary to estimate the functional radiative source term $\Phi_{\mathcal{L}}[j]$. Each element of this list stored the number of times a path ended with a given radiative index $j \in \{0, ..., N_{\text{nodes}}\}$.

[2] $N_{\text{nodes}} - 1$ radiative mesh added to the two fictive mesh of the left boundary $j = 0$ and the right boundary $j = N_{\text{nodes}}$.

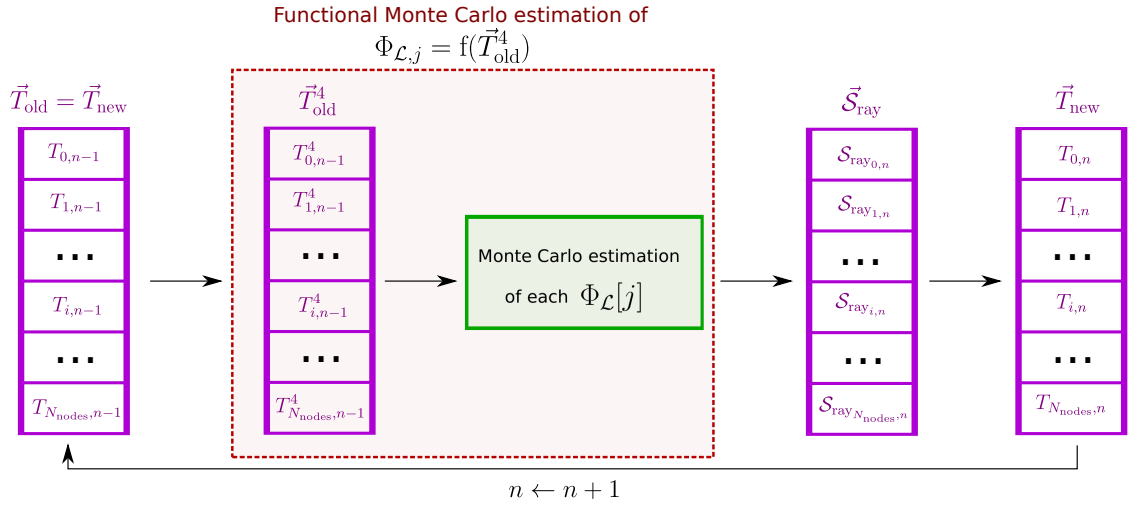

Figure 5: Scheme representing the n$^{\text{th}}$ iteration of the finite difference scheme coupled to the two different Monte Carlo algorithm. In the green square is represented the *classic* Monte Carlo estimation of each of the $N_{\text{nodes}} - 1$ radiative source terms at each iteration of the finite differences algorithm. In the red square is represented the functional estimation of the radiative source term enabling the use of the function at each iteration of the finite differences algorithm. The functional radiative source term is estimated with a *single* Monte Carlo computation before the finite differences algorithm.

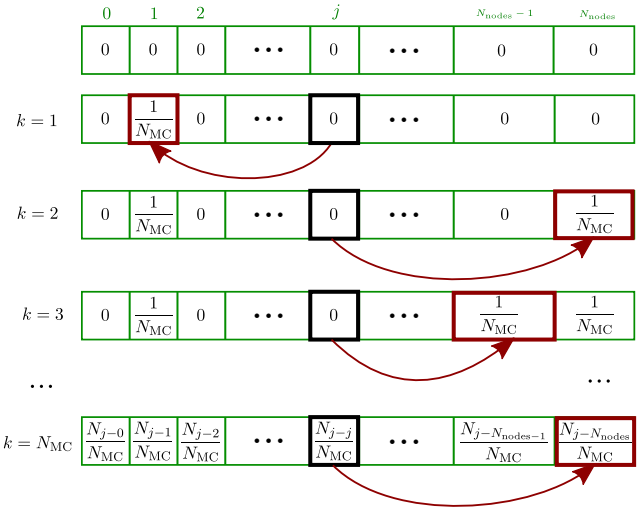

Figure 6: Illustration of the functional estimation Monte Carlo algorithm with the information stored at each k^{th} path sampling to build the function's coefficients. The path starts in the j^{th} mesh element (framed in black) and finishes in an other mesh element (framed in red), hence the information stored is the $j_{\text{end},k}$ index corresponding to the path's end mesh element.

- Firstly, the m_j values are initialized equal to zero (represented with the green framed vector in Fig. 6).
- Then, after the first realization, $k = 1$, as the path ends in the radiative mesh index $j = 1$, the counter at the location $m_j[1]$ is increased by a value equal to $\frac{1}{N_{\mathrm{MC}}}$.
- Similarly, for each of the following realizations $k = 2$ and $k = 3$, counters in the corresponding path end radiative indices are updated, of respectively $\frac{1}{N_{\mathrm{MC}}}$ in $m_j[N_{\text{nodes}}]$ and $\frac{1}{N_{\mathrm{MC}}}$ in $m_j[N_{\text{nodes}}-1]$. This procedure goes on for each realization k out of the total N_{MC} realizations, until the last one in this example in which for $k = N_{\mathrm{MC}}$, the last index $m_j[N_{\text{nodes}}]$ is incremented of $\frac{1}{N_{\mathrm{MC}}}$ (at least two realizations ended up with this index).

At the end of the single Monte Carlo computation, the output estimation m_j is a list made of $N_{\text{nodes}}+1$ coefficients, each of them counting how many times the path starting at the $j \equiv \mathrm{j}_{\text{start}}$ index ended in the j_{end} index. In the case of the previous example, the second part (⋆) of Eq. (18) may be reformulated as the following:

$$\begin{aligned}&\frac{1}{N_{\mathrm{MC}}}\sum_{k=1}^{N_{\mathrm{MC}}} T^4[j_{\text{end},k}] = \\ &\frac{1}{N_{\mathrm{MC}}}\sum_{k=1}^{N_{\mathrm{MC}}} (\mathcal{H}(j_{\text{end},k}=0)T^4_{\text{left}} + \mathcal{H}(j_{\text{end},k}=1)T^4_1 + \dots \\ &\dots + \mathcal{H}(j_{\text{end},k}=N_{\text{nodes}})T^4_{\text{right}})\end{aligned} \tag{19}$$

In which $\mathcal{H}$ is the Heaviside function equal to 1 if the condition is satisfied and 0 otherwise. For the first term, at the end of the k^{th} path, if $j_{\text{end},k} = 0$, $\mathcal{H}$ is equal to 1. Then,

$$\begin{aligned}&\frac{1}{N_{\mathrm{MC}}}\sum_{k=1}^{N_{\mathrm{MC}}} T^4[j_{\text{end},k}] = \\ &\frac{1}{N_{\mathrm{MC}}}\left(N_{\mathrm{j_{start}}-0}T^4_{\text{left}} + N_{\mathrm{j_{start}}-1}T^4_1 + \dots + N_{\mathrm{j_{start}}-N_{\text{nodes}}}T^4_{\text{right}}\right) \\ &= \sum_{\mathrm{j_{end}}=0}^{N_{\text{nodes}}} \frac{N_{\mathrm{j_{start}}-\mathrm{j_{end}}}}{N_{\mathrm{MC}}} T^4[\mathrm{j_{end}}]\end{aligned}$$

(20)

In this fashion, the latter expression can be transformed so that counters $N_{\mathrm{j_{start}}-\mathrm{j_{end}}}$ hold the number of times a path ended in a mesh element $\mathrm{j_{end}}$ during the Monte Carlo computation. For example, $N_{\mathrm{j_{start}}-0}$ holds the number of paths that terminated in the mesh element indexed with $j \equiv \mathrm{j_{end}} = 0$ out of the total of N_{MC} paths sampled.

The following reformulation is achieved by incorporating the previous developments of Eq. (19) into Eq. (18):

$$\Phi_L[\mathrm{j_{start}}] \approx 4k_a\sigma_{\mathrm{SB}}\delta_x \left(T^4[\mathrm{j_{start}}] - \sum_{\mathrm{j_{end}}=0}^{N_{\mathrm{nodes}}} \frac{N_{\mathrm{j_{start}}-\mathrm{j_{end}}}}{N_{\mathrm{MC}}} T^4[\mathrm{j_{end}}] \right) \tag{21}$$

Each coefficient $\frac{N_{\mathrm{j_{start}}-\mathrm{j_{end}}}}{N_{\mathrm{MC}}}$ is estimated at once with a single Monte Carlo computation. Actually all of the $N_{\mathrm{nodes}} - 1$ computations of the source term can be made at once with a single Monte Carlo computation[3], giving the following function :

$$\begin{pmatrix} \vec{\nabla}\cdot\vec{q}_{\mathrm{R}}[N_{\mathrm{nodes}}-1] \\ \cdots \\ \vec{\nabla}\cdot\vec{q}_{\mathrm{R}}[2] \\ \vec{\nabla}\cdot\vec{q}_{\mathrm{R}}[1] \end{pmatrix} = 4k_a\sigma_{\mathrm{SB}}\delta_x \times \begin{pmatrix} T^4[N_{\mathrm{nodes}}-1] \\ \cdots \\ T^4[2] \\ T^4[1] \end{pmatrix} \cdots$$
$$\cdots - \sum_{\mathrm{j_{end}}=0}^{N_{\mathrm{nodes}}} \begin{pmatrix} m[N_{\mathrm{nodes}}-1-\mathrm{j_{end}}]T^4[\mathrm{j_{end}}] \\ \cdots \\ m[2-\mathrm{j_{end}}]\,T^4[\mathrm{j_{end}}] \\ m[1-\mathrm{j_{end}}]\,T^4[\mathrm{j_{end}}] \end{pmatrix} \tag{22}$$

All of the coefficients m_{ij} (with $i \in [1, N_{\mathrm{nodes}} - 1]$ and $j \in [0, N_{\mathrm{nodes}}]$) of the source term estimated function with the single Monte Carlo computation can be gathered in a $(N_{\mathrm{nodes}} - 1) \times N_{\mathrm{nodes}} + 1$ matrix $\mathcal{M} \equiv \mathcal{M}_{IJ}$ expressed as follows :

$$\mathcal{M} = \begin{pmatrix} \frac{N_{(N_{\mathrm{nodes}}-1)-\mathrm{left}}}{N_{\mathrm{MC}}} & \cdots & \frac{N_{(N_{\mathrm{nodes}}-1)-(N_{\mathrm{nodes}}-1)}}{N_{\mathrm{MC}}} & \frac{N_{(N_{\mathrm{nodes}}-1)-\mathrm{right}}}{N_{\mathrm{MC}}} \\ \vdots & \cdots & & \vdots \\ \frac{N_{2-\mathrm{left}}}{N_{\mathrm{MC}}} & \cdots & \frac{N_{2-(N_{\mathrm{nodes}}-1)}}{N_{\mathrm{MC}}} & \frac{N_{2-\mathrm{right}}}{N_{\mathrm{MC}}} \\ \frac{N_{1-\mathrm{left}}}{N_{\mathrm{MC}}} & \cdots & \frac{N_{1-(N_{\mathrm{nodes}}-1)}}{N_{\mathrm{MC}}} & \frac{N_{1-\mathrm{right}}}{N_{\mathrm{MC}}} \end{pmatrix} \tag{23}$$

These m_{ij} coefficients can be viewed as volumetric view factors that determine how each element of the radiative mesh views another. Similarly to the previous Monte Carlo estimation, the uncertainty s_{ij} of each radiative source term can be estimated as well as a function of the field of temperature to the fourth power, although no further details will be presented here.

The corresponding finite differences and functional Monte Carlo algorithm is detailed in the Algorithm 2.2.

Algorithm 2.2: Computation of the temperature profile $\vec{T}_{\mathrm{new}}$ with the finite differences and the functional Monte Carlo algorithm.

for $j = 1 : N_{\mathrm{nodes}} - 1$ **do**
  Estimation of the $\mathcal{M}$ with the Monte Carlo computation (see Eq. (23))
end
while $\varepsilon >$ tolerance **do**
  $\vec{T}_{\mathrm{old}} = \vec{T}_{\mathrm{new}}$ *%Initialization*
  for $j = 1 : N_{\mathrm{nodes}} - 1$ **do**
    Computation of $\vec{\nabla}\cdot\vec{q}_{\mathrm{R}}[j]$ (see Eq. (22))
  end
  for $i = 0 : N_{\mathrm{nodes}} - 1$ **do**
    for $j = 1 : N_{\mathrm{nodes}} - 1$ **do**
      Calculation of $S_{\mathrm{ray}}[i]$ (see Eq. (9))
    end
    Calculation of each $\vec{T}_{\mathrm{new}}[i]$ (see Eq. (8))
    $\varepsilon \mathrel{+}= \frac{||\vec{T}_{\mathrm{new}}[i]-\vec{T}_{\mathrm{old}}[i]||}{\vec{T}_{\mathrm{new}}[i]}$
  end
end

Both of these Monte Carlo-finite differences (see Algorithm 2.1) and functional Monte Carlo-finite differences (see Algorithm 2.2) algorithms are applied to the three different tests cases and validated in comparison with the semi-analytical solutions from Viskanta et al. in the next section. These algorithms are implemented in `C` language in Star-CoRad calculation code [36] thanks to the `star-engine` libraries[4].

3. Results and Discussion

Three distinct Viskanta et al. problems are investigated; they were previously depicted collectively in Fig. 1. The two first problems correspond to a pure absorbing/emitting medium with black walls [46] and then with gray walls [45], each of them are studied in the following Sec. 3.1 and Sec. 3.2. The last problem is an absorbing/emitting and scattering medium with black walls [44] and is detailed in Sec. 3.3. In each of these cases, conduction is at steady state and radiation within the volume. Temperature profiles are computed for different parameters values as shown below. The research data repository [10] contains all of the data used to generate the results of this article.

[3] Only $N_{\mathrm{nodes}} - 1$ radiative source term are estimated, as the radiative source term of the two boundary mesh elements in $j = 0$ and $j = N_{\mathrm{nodes}}$ are not needed.

[4] https://www.meso-star.com/projects/star-engine/star-engine.html

3.1. Validation in a pure absorbing medium with black walls

A pure gray absorbing medium $\mathcal{D}$ with black walls ($\epsilon_{\text{left}} = \epsilon_{\text{right}} = 1$) is considered in the first scenario. To quantify the relative contribution of conduction and radiation, a dimensionless parameter, the Stark number (also known as the conduction–radiation parameter) is introduced and expressed as:

$$\mathcal{N} = \frac{\lambda\, k_{\text{a}}}{4\sigma_{\text{SB}} T_{\text{right}}^3} \tag{24}$$

Given a certain value of the temperature T_{right} corresponding to the hot temperature of the plate, the fact that $k_{\text{a}} = 1\ \text{m}^{-1}$ and the plate thickness $L = 1\,\text{m}$ leads to an optical thickness equal to $\tau = \beta L = k_{\text{a}} L = 1$. Thus, when the Stark number value is set, the thermal conductivity value λ is inferred as presented in Eq. (25).

$$\lambda = \frac{\mathcal{N} 4\sigma_{\text{SB}} T_{\text{right}}^3}{k_{\text{a}}} \tag{25}$$

For large values of $\mathcal{N}$, conduction predominates and on the opposite, for small values of $\mathcal{N}$, radiation is the most important energy transport phenomenon.

In total, three values of the Stark number $\mathcal{N}$ are chosen; two cases values for which radiation dominates conduction more or less strongly emphasizing non-linearities behavior on the temperature profile, i.e. for $\mathcal{N} = 0.01$ and $\mathcal{N} = 0.1$; one value for which conduction predominates radiation and the linear temperature profile is retrieved, i.e. $\mathcal{N} = 1$. For each of these Stark Number values, results are computed and presented in the case of the pure absorbing medium with black walls in Fig. 7.

Two cases are studied for two different values of temperature ratios. For each of these temperature ratios, temperature profiles and relative errors profiles are presented, in Fig. 7a and Fig. 7b for the $T_{\text{right}} = 2 \times T_{\text{left}}$ case and in Fig. 7c and Fig. 7d in the $T_{\text{right}} = 10 \times T_{\text{left}}$ case.

The relative error $\mathbf{e_r}$ is calculated such as:

$$\mathbf{e_r} = \left| \frac{T_{\text{vis}} - T_{\text{FD-FMC}}}{T_{\text{vis}}} \right| \tag{26}$$

The latter expression of the relative error is arbitrary and in which T_{vis} stands for the temperature value from Viskanta et al. and $T_{\text{FD-FMC}}$ is the temperature value computed with the finite differences–functional Monte Carlo algorithm.

For both of the temperature ratios, the finite differences–functional Monte Carlo (FD–FMC) results (represented in black empty symbols on Figs. 7a and 7c) overlap accurately the finite differences–Monte Carlo (FD–MC) results (represented in red, orange and green filled bullets), as it should be because there is no valuable reason for them to differ. Also, all of the results from the two latter algorithms are in good agreement with results from the semi-analytical solution of Viskanta & Grosh [46] represented in black continuous, dashed and dotted lines. In order to go further, one may notice that relative errors, as expressed in Eq. (26) do not exceed respectively 1% and 1.5% for $\mathcal{N} = 0.1, 1$ and $\mathcal{N} = 0.01$ in case of the $T_{\text{right}} = 2 \times T_{\text{left}}$ ratio (see Fig. 7b) and, in the case with more non linearities with $T_{\text{right}} = 10 \times T_{\text{left}}$, the relative error does not exceed 3% for $\mathcal{N} = 0.1, 1$ and 8% when $\mathcal{N} = 0.01$, which is the extreme case for non linearities (see Fig. 7d). The maximum values of relative errors are in the case where non–linearities are greatest, i.e. where radiation dominates conduction ($\mathcal{N} = 0.01$), in mesh elements with the most intense temperatures gradients, for the values of optical thickness comprised between 0 and 0.1, which are 1.4% and 8% of relative error for respectively the first (see Fig. 7b) and second temperature ratio (see Fig. 7d).

3.2. Validation in a pure absorbing medium with gray walls

In the second test case from Viskanta & Grosh [45], the same configuration as in the first test case is considered, but with gray walls ($\epsilon_{\text{left}} = \epsilon_{\text{right}} < 1$). For a value of the Stark number set to $\mathcal{N} = 0.01$ and a temperature ratio corresponding to $T_{\text{right}} = 2 \times T_{\text{left}}$, different values of walls emissivities are chosen. Three cases are considered with: $\epsilon_{\text{left}} = \epsilon_{\text{right}} = 1$ (corresponding to the previous black walls case), $\epsilon_{\text{left}} = \epsilon_{\text{right}} = 0.5$ and $\epsilon_{\text{left}} = \epsilon_{\text{right}} = 0.1$. As before, the FD–FMC results (represented in black empty symbols in Fig. 8a) perfectly overlap the FD–MC results (represented in red, purple and blue filled bullets) and these results are in good agreement with the semi-analytical results from Viskanta & Grosh [45] represented in dotted and dashed lines.

Considering error profiles, as represented in Fig. 8b, the maximum values are between 2.5% and 3% for low emissivity values ($\epsilon_{\text{left}} = \epsilon_{\text{right}} = 0.1$ which means very reflective walls) when temperature gradients are the greatest. Otherwise, for other emissivity values and when temperature gradients are more moderate, the average relative error is approximately 0.5%.

3.3. Validation in an absorbing and scattering medium with black walls

A black absorbing and scattering medium $\mathcal{D}$ bounded by black walls is considered ($\epsilon_{\text{left}} = \epsilon_{\text{right}} = 1$). Viskanta et al. [44] defined another Stark dimensionless number $\mathcal{N}'$. This number is the inverse of to the previous Stark number $\mathcal{N}$ from Eq. (27), but taking into account scattering effects :

$$\mathcal{N}' = \frac{4\sigma_{\text{SB}}\, T_{\text{right}}^3}{\lambda\, \beta} = \frac{4\sigma_{\text{SB}}\, T_{\text{right}}^3}{\lambda\, (k_a + k_s)} = \frac{1}{\mathcal{N}} \tag{27}$$

For the sake of uniformity, we consider here $\mathcal{N}$ from Eq. (27) as the only definition of the Stark number. As a result, the values of the Stark number $\mathcal{N}'$ from [44] are converted to be consistent with the Stark number $\mathcal{N}$. In the extreme values, $\mathcal{N}' = 0 \Rightarrow \mathcal{N} = \infty$ indicates that heat

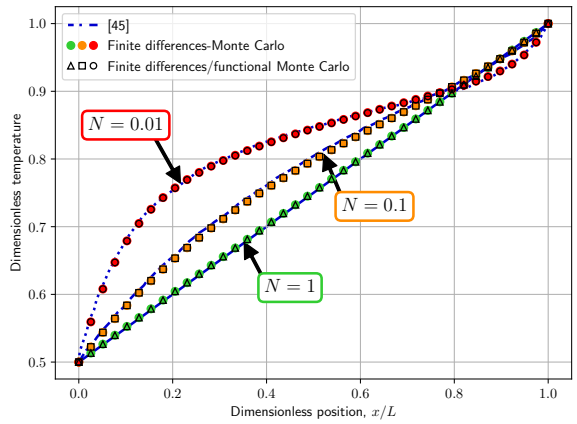

(a) Influence of the Stark number $\mathcal{N}$ on the temperature profile for $T_{\text{right}} = 2 \times T_{\text{left}}$ [46].

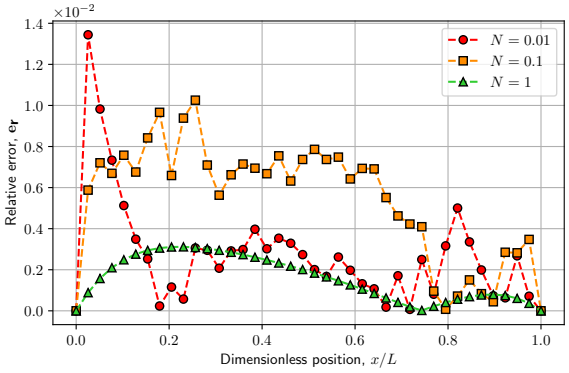

(b) Corresponding error profiles for different values of $\mathcal{N}$ in the case of $T_{\text{right}} = 2 \times T_{\text{left}}$.

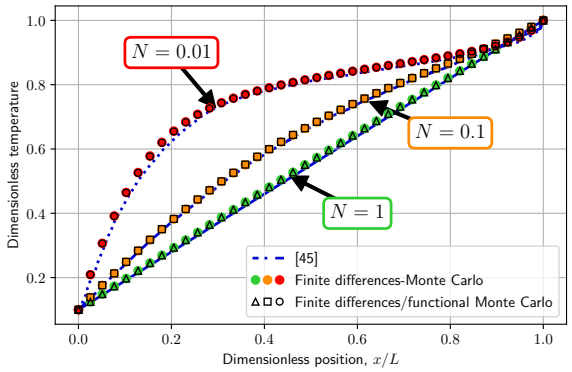

(c) Influence of the Stark number $\mathcal{N}$ on the temperature profile for $T_{\text{right}} = 10 \times T_{\text{left}}$ [46].

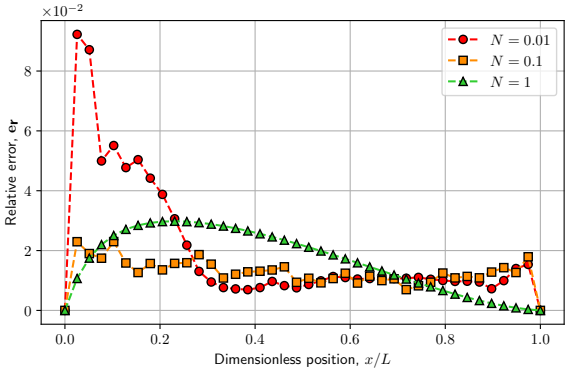

(d) Corresponding error profiles for different values of $\mathcal{N}$ in the case of $T_{\text{right}} = 10 \times T_{\text{left}}$.

Figure 7: Dimensionless temperature distribution $\theta(\tau)) = T(\tau)/T_{\text{right}}$ with optical thickness τ for three different values of the Stark number $\mathcal{N} = \{0.01, 0.1, 1\}$ in the case of the pure absorbing medium with black walls.

transfer is governed solely by conduction and $\mathcal{N}' = \infty \Rightarrow \mathcal{N} = 0$ indicates that heat transfer is only governed by radiation. In the present case, the Stark number is set equal to $\mathcal{N} = 0.1 \Leftrightarrow \mathcal{N}' = 10$, corresponding to a configuration where radiation dominates. Two sub-cases are considered in which $T_{\text{right}} = 2 \times T_{\text{left}}$ and $T_{\text{right}} = 10 \times T_{\text{left}}$. For each of these different temperature ratios, three different values of the scattering albedo k_s/β are chosen: $k_s/\beta = 0$, $k_s/\beta = 0.5$ and finally $k_s/\beta = 1$ (pure scattering medium).

The FD–FMC results (represented in black empty symbols in Fig. 9a) are overlapping the FD–MC results (represented in orange, yellow and green bullet filled symbols). Both of the latter results are in good agreement with the semi-analytical results from Viskanta [44] represented in continued, dashed and dotted lines in fig. 9a. In terms of error profiles, relative errors at the lowest temperature ratio, $T_{\text{right}} = 2 \times T_{\text{left}}$, are relatively low, with a maximum error value of approximately 0.6% (see Fig. 9b). In the case of the maximum temperature ratio, $T_{\text{right}} = 10 \times T_{\text{left}}$, the relative error does not exceed 2%.

3.4. Computational time benefit of the FEMC algorithm

As previously introduced in Sec. 2.5, one of the major benefit of the FD–FMC algorithm is to enable a significant computational time reduction compared to the original FD–MC algorithm. In cases when only the temperature list $\vec{T}^4_{\text{old}}$ values change as input of the functional Monte Carlo algorithm to estimate the radiative source term, the function can be estimated once for all and re-used in the post-treatment process to estimate the temperature profile for different values of the parameters (see Fig. 5). More specifically, this means that to estimate the 15 temperature profiles presented in Fig. 7, Fig. 8 and Fig. 9, only 7 radiative source term functions needed to be estimated with a functional Monte Carlo computation, as detailed in Fig. 10.

For instance, the radiative source term function 1 estimated in the case of a pure absorbing medium in which, $\mathcal{N} = 0.01$, both walls are black ($\epsilon_{\text{left}} = \epsilon_{\text{right}} = 1$) and the temperature ratio is equal to $T_{\text{right}} = 2 \times T_{\text{left}}$ can be used to estimate obviously the temperature profile in this specific case 1 and also in the case of a different temperature ratio,

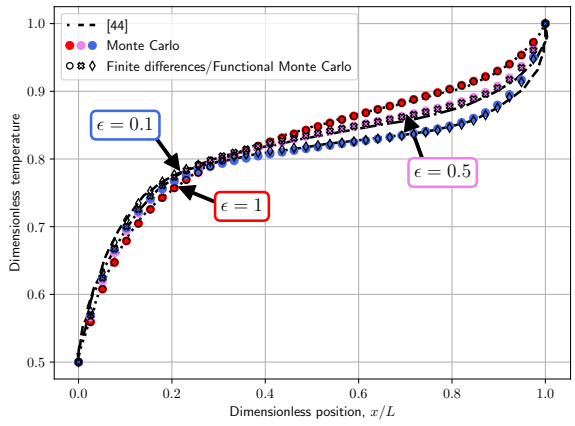

(a) Influence of wall emissivity value $\epsilon_{\text{left}} = \epsilon_{\text{right}}$ on the temperature profile for $\mathcal{N} = 0.01$ (see [45]).

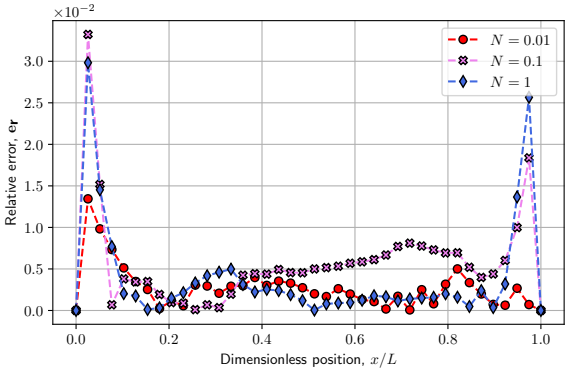

(b) Corresponding error profiles for different emissivity values $\epsilon_{\text{left}} = \epsilon_{\text{right}}$.

Figure 8: Dimensionless temperature distribution $\theta(\tau)) = T(\tau)/T_{\text{right}}$ with optical thickness τ for different emissivities values $\epsilon_{\text{left}} = \epsilon_{\text{right}} = \{0.1, 0.5, 1\}$ in the case of the pure absorbing medium with grey walls.

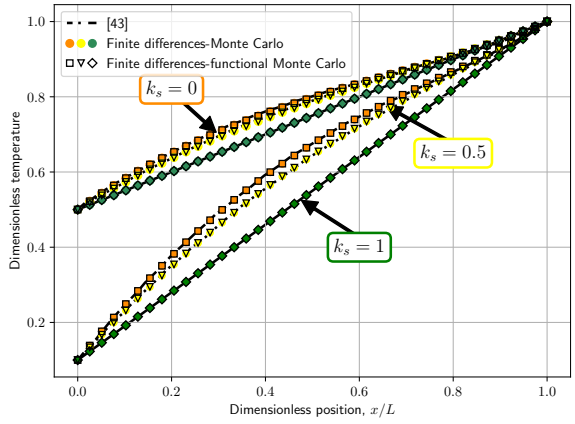

(a) Influence of the albedo k_s/β on the temperature distribution for $\mathcal{N} = 0.1$ $\epsilon_{\text{left}} = \epsilon_{\text{right}} = 1$ (see [44]).

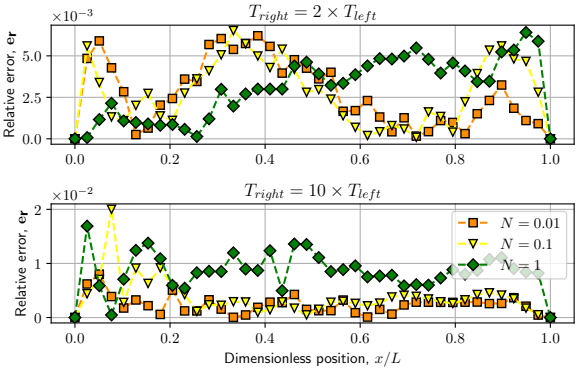

(b) Corresponding error profiles for different values of the scattering albedo k_s/β for both temperature ratios.

Figure 9: Variation of dimensionless temperature distribution $\theta(\tau)) = T(\tau)/T_{\text{right}}$ with optical thickness τ in the case of the absorbing–scattering medium with black walls for different scattering albedo values $k_s/\beta = \{0, 0.5, 1\}$.

as in the case 2 for $T_{\text{right}} = 10 \times T_{\text{left}}$. Similarly, the radiative source term function 3 estimated in the case of a pure absorbing medium in which, $\mathcal{N} = 0.1$ with black walls and a temperature ratio corresponding to $T_{\text{right}} = 2 \times T_{\text{left}}$ can be used to estimate the temperature profile for this case 3, as well as for the temperature ratio equal to $T_{\text{right}} = 10 \times T_{\text{left}}$ 4. This function can also be used to estimate the temperature profile in the case of the absorbing/emitting and scattering medium where $k_s = 0$, for the two different temperature ratio of $T_{\text{right}} = 2 \times T_{\text{left}}$ 5 and $T_{\text{right}} = 10 \times T_{\text{left}}$ 6 because the Stark number value $\mathcal{N}'$ in this specific case where $k_s = 0$ is equivalent to the Stark number defined in one of the pure absorption case : $\mathcal{N}' = 10 \equiv \mathcal{N} = 0.1$.

The same applies to the five remaining source term functions to estimate, i.e. 7, 9, 10, 11 and 13, which are then reused to estimate the temperature profiles in the cases 7 – 14 (eight cases in total[5]).

In order to compare the computation times of the FD–MC algorithm and the FD–FMC algorithm, constraints needed to be settled of the tolerance criterion ε of the finite differences algorithm as well as on the relative error based on the estimated uncertainties s and s^S values for respectively the Monte Carlo and functional Monte Carlo algorithms. In consequence, the maximum tolerance criterion ε value was set to 0.001. Both relative errors m/s and m_{ij}/s_{ij} maximum values were set equal to 5 %, which is the value at which a Monte Carlo estimation is deemed to be sufficiently accurate,

[5]Out of the total fifteen plots and cases, one is missing, the one corresponding to Fig. 8a in which $\mathcal{N} = 0.01$, walls are black and the temperature ratio is equal to $T_{\text{right}} = 2 \times T_{\text{left}}$. This case was on purpose not represented in Fig. 5 as it is strictly equivalent to the case 1.

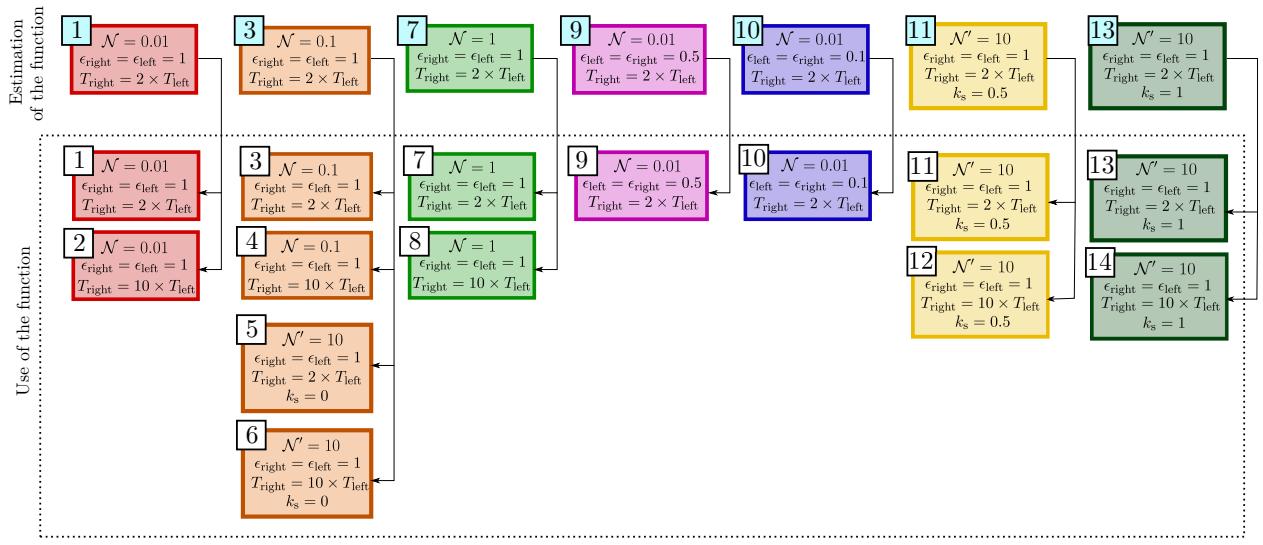

Figure 10: Scheme representing the seven radiative source term functions for each of the seven test cases.

and to achieve this accuracy, each number N_{MC} of Monte Carlo and functional Monte Carlo computations is adjusted accordingly. Each temperature profile computed consists in 40 conductive nodes.

The average time required to estimate a function using the functional Monte Carlo approach is 6 s, while the time required to estimate a temperature profile comprised of 40 conductive nodes is only a few milliseconds. Through using the FD–MC algorithm, the time required to estimate a temperature profile consisting of 40 conductive nodes for each of the fifteen examples from around 30 s (in the case 7) to 4 min (in the case 3). In the case of a pure scattering medium (case 12), the computing time is less than one second. On the other hand, in the case of a pure absorbing medium with a temperature ratio of $T_{right} = 10 \times T_{left}$ and $\mathcal{N} = 0.1$ (case 4), the computation time is greater than 7 min. The detail of each computation time for the fifteen different cases is given in Appendix C.

For estimating a temperature profile, the greatest benefit of the FD–FMC algorithm over the FD–MC is the time savings. If the radiative source term functions must be calculated with the FD–FMC algorithm before being used to estimate the temperature profiles, the functional algorithm is approximately 20 to 40 times faster than the FD–MC algorithm. If the functions have already been calculated and solely need to be used in the finite differences algorithm of the FD–FMC algorithm, the later algorithm is around 10^2 to 10^3 times faster than the other algorithm.

Ultimately, in the three reference configurations from Viskanta et al. [46, 45, 44], the function estimation and use of the radiative source term $\vec{\nabla}\cdot\vec{q}_R$ depending on the temperature list to the power 4 proved to be accurate in comparison with the semi-analytical results. In the current examples, the functional computation can therefore be faithfully utilized in place of the original Monte Carlo algorithm for inversion processes requiring a significant number of direct model calls. Obviously, these configurations are purely academic; however, they already possess cumbersome characteristics that must accurately considered (i.e. the coupling between conduction and volumetric radiation, the uniform scattering nature of the medium etc.) and for these reasons, the feasibility of the finite differences–functional Monte Carlo algorithm to estimate the radiative source term as a function of the temperature list has been established.

All simulations using the functional Monte Carlo algorithm were carried out using the freely available Star-CoRad calculation code [36]. This code also enables the execution of additional simulations based on the user's preferences values for the following parameters: boundary temperatures T_{left} and T_{right}, walls emissivities $\epsilon_{left} = \epsilon_{right}$, optical parameters k_a et k_s and optical thickness τ.

4. Informations contained in the functions coefficients $\mathcal{M}$

The coefficient values of a function can be provided in matrix form and represented by a colormap depicting the magnitude of each coefficient. In each of these images, a cell corresponds to the probability $\frac{N_{I-J}}{N_{MC}}$ that a ray emitted from I (the starting cell) is absorbed by cell J (the finishing cell)[6]. For all of the aforementioned results, there were 40×40 conductive nodes in addition to the 2 conductive nodes on the walls, one on the left and one on the right. Therefore, there were 39×39 radiative nodes in addition to 2 boundary nodes. These are the 40×40 coefficients that correspond to the radiative cell coefficients shown on Fig. 11.

[6] In fact, the sum of each row of the matrix's coefficients equals to 1, indicating that these proportions of rays are homogeneous with probabilities.

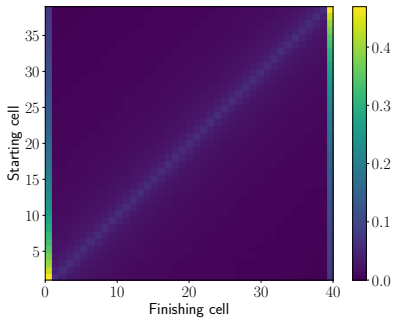

(a) Cases 1 and 2, where $\mathcal{N} = 0.01$ and walls are black.

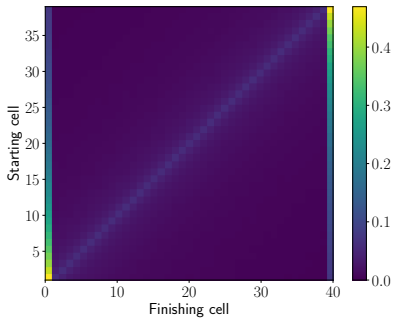

(b) Cases 3 and 4, where $\mathcal{N} = 0.1 \equiv \mathcal{N}' = 10$ and walls are black.

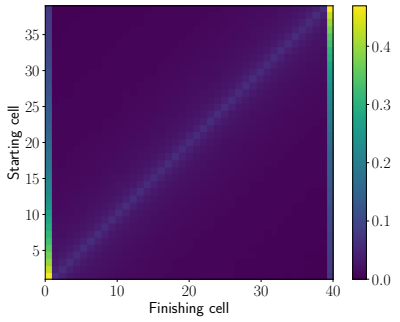

(c) Cases 5 and 6, where $\mathcal{N} = 0.1 \equiv \mathcal{N}' = 10$ and walls are black.

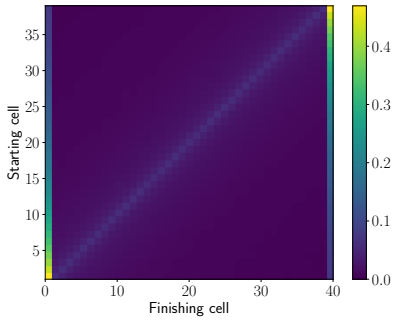

(d) Cases 7 and 8, where $\mathcal{N} = 1$ and walls are black.

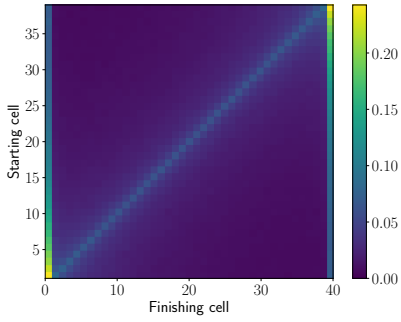

(e) Case 9 where $\mathcal{N} = 0.01$ and walls are gray with $\epsilon_{\text{left}} = \epsilon_{\text{right}} = 0.5$.

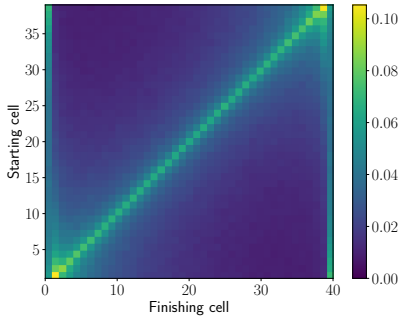

(f) Case 10 where $\mathcal{N} = 0.01$ and walls are gray with $\epsilon_{\text{left}} = \epsilon_{\text{right}} = 0.1$.

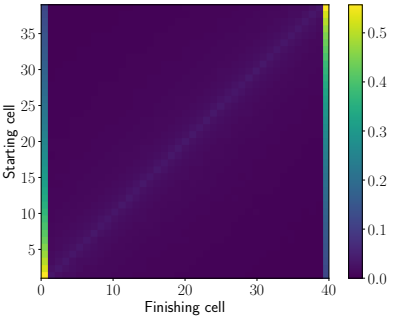

(g) Cases 11 and 12, where $\mathcal{N}' = 10$, walls are black and $k_s = 0.5$.

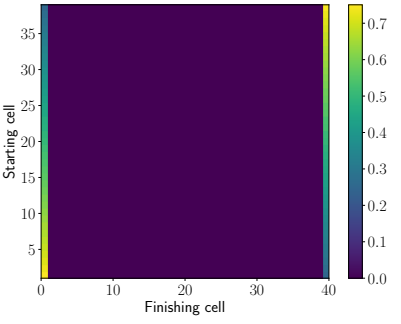

(h) Cases 11 and 12, where $\mathcal{N}' = 10$, walls are black and $k_s = 1$.

Figure 11: Examples of $\mathcal{M} \equiv \mathcal{M}_{IJ}$ matrices of the function's coefficients.There are $I \times J = 39 \times 39$ radiative cells added to the two boundaries, where I stands for the *Starting cell* and J, the *Finishing cell*, hence a total of $39 \times 41 = 1599$ coefficients represented in each figure. (a)-(d) Pure absorbing media configuration with black walls ($\epsilon_{\text{left}} = \epsilon_{\text{right}} = 1$) ; (e)-(f) Pure absorbing media configurations with grey walls ; (g)-(f) Absorbing and scattering media configurations with black walls.

These coefficients provide analytical elements for a more thorough comprehension of the effect of specific thermophysical or geometric parameters on radiative exchange within a semitransparent medium. In general, it can be observed that under the simulation conditions guided by Viskanta literature cases [46, 45, 44], the matrices show symmetry. Furthermore, the exchange probabilities within these matrices display certain characteristics. Firstly, the probabilities are systematically distributed along the diagonal, suggesting that a cell denoted as I is more likely to exchange with itself rather than with another cell denoted as J. Secondly, the most significant values of exchange probabilities are found at the edges of the matrices, indicating that the cells experience maximum absorption of rays at the boundaries.

The observations made from Fig. 11a to Fig. 11d support the assumption that a radiative cell primarily interacts with itself (indicated by values around 0.2 along the diagonal of the matrices) and secondarily with the nearest boundary radiative cell (0.4 for cells in close proximity to a boundary, gradually decreasing towards cells located in the middle of the medium). The observed outcomes are expected, as they demonstrate that the mean estimated coefficients remain constant regardless of the Stark number, i.e. the proportion of conduction versus radiation. These findings hold true for cases involving a pure absorbing gray medium with black walls and a homogeneous absorption coefficient.

The evidence of influence becomes apparent only in the presence of gray walls. Undoubtedly, enhancing the degree of reflection at the boundary will result in alterations of the probabilities, as cells will show a greater propensity to exchange with themselves, while rays will experience reduced absorption at the boundaries. From a logical standpoint, it can be inferred that an increase in reflection results in a decrease in the likelihood of cell exchange with the boundaries. This relationship is illustrated in Fig. 11e, where a maximum value of 0.2 is observed when $\epsilon_{\text{left}} = \epsilon_{\text{right}} = 0.5$. In contrast, Fig. 11f demonstrates a maximum value of 0.1 when $\epsilon_{\text{left}} = \epsilon_{\text{right}} = 0.1$. In the aforementioned scenario, the likelihoods of self-exchange or exchange with the boundary are of comparable magnitude. In each case, it is observed that none of these elements demonstrate a tendency towards asymmetry, and the cells predominantly exchange with themselves. Ultimately, it can be observed that the presence of homogeneous scattering in the medium has a tendency to reduce the impact of "self-exchange". Moreover, it is noted that as the scattering coefficient increases, the likelihood of cell I exchanging with one of the boundaries also increases. For instance, when $k_s = 0.5$, the first radiative cell (represented by the pixel in the bottom left corner of Fig. 11g) has a probability of 0.5 to exchange with the left boundary. However, when $k_s = 1$, this probability increases to 0.7 (corresponding to the pixel in the bottom left corner of Fig. 11h).

It is crucial to have in mind the significant information that may be inferred from these coefficients, and consequently, from the estimation of these functions. The Monte Carlo method can be utilized to estimate the function coefficients, and it is possible to explicit the informations contained in the optical paths sampled by the algorithm. This allows for the derivation of analytical elements related to the physics of the situation being investigated. This methodology can be applied to geometrically or physically complicated applications, provided that the coefficients can be accurately determined. The probabilities and function coefficients were previously described and discussed in the study conducted by Zarrouati et al. [48]. In their work, they also found the presence of a symmetrical matrix in the case of a purely absorbing porous medium enclosed by black walls. It clearly showed that this symmetry derived from the principle of reciprocity of optical paths. In contrast to our case, there appeared to be a distinct probability distribution surrounding the diagonal values in this instance, potentially due to the heterogeneity of the radiative properties. Therefore, it would be of interest to expand our investigations to include configurations where the radiative properties also exhibit heterogeneity.

5. Conclusions

The present work demonstrated the development of a coupled conduction–radiation direct model for gray semitransparent media, on an academic configuration offering almost the only semi-analytical solutions in the literature [46, 45, 44]. The function estimation of the radiative source term of the heat equation with a FD–FMC algorithm resulted in a significant reduction in computation time compared to the original FD–MC algorithm used to estimate the same temperature profiles in the academic configurations, without sacrificing model accuracy.

On the matter of geometry or thermophysical parameters complexity, the present study is still a long way from practical configurations. Nevertheless, the provided methodology is a proof of practicality in academic configuration and shows promise for future developments to address more complex configurations. Regarding the application of the FD–FMC algorithm in inversion processes, the production of a fast direct model such as this one is crucial.

Nothing hinders the use of the latter algorithm to two or three-dimensional conduction–radiation coupled problems with transient heat conduction. In addition, this methodology will be used in the future to develop a direct model of the 2D or 3D configuration of the parallel hot wire apparatus, as previous research demonstrated the need for a robust direct coupled model to more accurately represent the effect of radiation on the transient evolution of temperature in complex heterogeneous medium under consideration [37].

Given the computation time enhancement of the FD–FMC algorithm, this algorithm would be interesting in the case of sensitivity studies preceding the inversion procedure. This direct model may be first applied to 2D/3D configurations as the computing environment is developed within the star-engine computer science library [29].Additionally,

the efficiency of computation times can be enhanced by the optimization of the *star-CoRad* program [36].

In the context of a classical Monte Carlo estimation of the radiative source term, incorporating spectral radiative properties, which involves sampling frequencies beyond a gray media assumption, is relatively straightforward. However, when it comes to estimating the transfer function that connects the radiative source term and the temperature field, the formalism involved in this task is considerably more laborious. This observation stems from the inclusion of temperature in the exponential term of the spectral blackbody intensity expression (see Eq. (5)). In order to surmount this constraint, which arises from the exponential non-linearity relationship, additional formal developments are necessary to calculate the radiative source term as a temperature field-dependent transfer function. This form of non-linearity is differentiated from the non-linearity relationship between the heat equation and the radiative source term when grey radiative properties are considered, which is dependent on T^4. The distinction arises due to the treatment of the two enunciated non-linearities differently in the context of Monte Carlo formalism. A similar formal effort to surmount the exponential function's non-linearity was undertaken previously in the Beer extinction law utilizing Null-Collisions algorithms [12, 5]; such an endeavor may be pursued in the future. After the removal of this restriction, it would be appropriate to explore the potential for enhancing the efficiency of algorithms through the implementation of ray-tracing optimizations such as *Optimized Emission Reciprocity Method* (OERM) [49, 41]. This approach aims to enhance both the accuracy and computational efficiency of inversion processes.

Furthermore, the utilization of Null-Collision Algorithms can be as well employed to expand the existing method to incorporate heterogeneous radiative properties. Indeed, to effectively consider media with spatially heterogeneous properties, the Null-Collision formalism suggested by Galtier et al. can be employed for an accurate analysis [12, 9]. The utilization of this approach results in computational efficiency and the simplification of equations, as it does not rely on a mesh structure, and consequently, it facilitates the execution of highly detailed simulations involving heterogeneous media [16]. Subsequently, in a manner akin to the findings presented in Royer et al. [39], the radiative source term in the heat equation may be estimated as a linear function that is dependent upon the temperature field raised to the power of four. Nevertheless, when dealing with strongly heterogeneous media, the current approach would encounter certain limits. This is due to the fact that the assumption of a homogeneous medium, the assumption behind Beer's law, would no longer hold true, necessitating the resolution of the Generalized Radiative Transfer Equation (RTE). In the study conducted by Zarrouati et al. [48], it was demonstrated that the aforementioned constraint can be overcome in situations where semi-transparent material with absorbing/emitting and scattering properties are present.

An additional limitation of the FD/FMC method is its inability to take into account situations in which radiative properties are depending on temperature. In this scenario, it is clear that the Monte Carlo algorithm necessitates the knowledge of local temperature information for each optical path. Consequently, the independence of each optical path from the temperature field is compromised, thereby precluding the estimation of the radiative source term as a linear function of the temperature field raised to the power of four.

Acknowledgments

The authors would like to thank the CNRS joint laboratory Canopée and Saint–Gobain Research Paris for initiating the project and funding the post-doctoral support, as well as the star-engine library [29] for enabling the development of the coupled heat transfer algorithms thanks to the computational Monte Carlo libraries and the Meso-centre Explor [43] for providing the necessary computational resources for the execution of these algorithms. High Performance Computing resources were partially provided by the EXPLOR centre hosted by the University de Lorraine (Project : 2020EMPPX2210).

A. Estimation of the spectral radiative intensity $\mathcal{I}_\nu(\vec{x}, \vec{\omega})$

Radiative transfer can be formulated as a Fredholm-type integral equation of the first kind, and due to this formulation, formal developments can be constructed to carry out the resolution using Monte Carlo methods.

A.1. Integral formulation of the RTE

In fact, the RTE expressed in differential form Eq. (6) with absorption and scattering events can be reformulated as an integral equation (see Fig. 12).

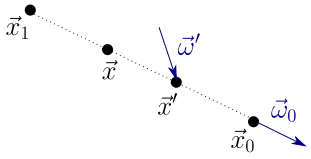

Figure 12: The notations employed for the differential-integral transition of the RTE: The radiative itensity is sought at a location $\vec{x}_0$ and direction $\vec{\omega}_0$, to do so, contributions such as the attenuation by extinction (absorption and diffusion) may occur along this same direction from a location $\vec{x}_1$, reinforcement by emission can occur at a location $\vec{x}$ between $\vec{x}_1$ and $\vec{x}_0$ or reinforcement by scattering can occur at a location $\vec{x}'$ from a direction $\vec{\omega}'$. [26]

The spectral radiative intensity $\mathcal{I}_\nu(\vec{x}_0, \vec{\omega}_0)$ can be expressed by integrating the RTE from Eq. (6) between two locations $\vec{x}_1$ and $\vec{x}_0$ along the direction $\vec{\omega}_0$, expressed as $\vec{x}_0 =$

$\vec{x}_1 + ||\vec{x}_1 - \vec{x}_0||\vec{\omega}_0$ [26]. In the case of homogeneous radiative properties, this operation yields the following result:

$$\begin{aligned}\mathcal{I}_\nu(\vec{x}_0,\vec{\omega}_0) &= \mathcal{I}_\nu(\vec{x}_1,\vec{\omega}_0)e^{\beta_\nu||\vec{x}_1-\vec{x}_0||} \\ &+ \int_0^{||\vec{x}_1-\vec{x}_0||} k_{a,\nu}\mathcal{I}_\nu^{eq}(T(\vec{x}))e^{\beta_\nu||\vec{x}-\vec{x}_0||}dl \\ &+ \int_0^{||\vec{x}_1-\vec{x}_0||} k_{s,\nu}\left(\int_{4\pi} \mathrm{P}_{sca,\nu}(\vec{x},\vec{\omega}'|\vec{\omega}_0)\mathcal{I}_\nu(\vec{x},\vec{\omega}')d\vec{\omega}'\right)e^{\beta_\nu||\vec{x}-\vec{x}_0||}dl\end{aligned} \tag{28}$$

The first element of the aforementioned equation represents the attenuation of absorption and scattering, also known as extinction, that occurs between the points $\vec{x}_1$ and $\vec{x}_0$ in the direction of $\vec{\omega}_0$. The second term relates to the reinforcement through emission, whereas the last term refers to the reinforcement by scattering.

A.2. Spectral radiative intensity in an absorbing and scattering semi-infinite medium

In order to solve the above equation Eq. (28) using the Monte Carlo method, it is necessary to reformulate it in a statistical fashion. The integral from 0 to $||\vec{x}_1 - \vec{x}_0||$ can be equivalently expressed as an integral over $\mathbb{R}^+$ by employing the Heaviside function $\mathcal{H}$[7].

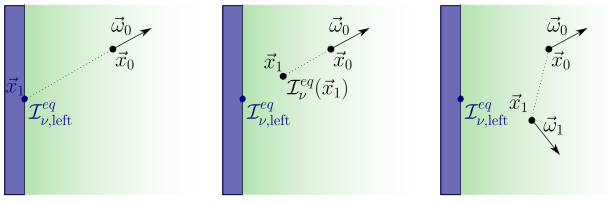

Figure 13: Different examples of contribution to the radiative intensity calculated at a location $\vec{x}_0$ and direction $\vec{\omega}_0$; (*left*) - Reinforcement due to radiation emitted at the boundary $\mathcal{I}^{eq}_{\nu,\text{left}}$ and attenuated along the path ; (*center*) - Reinforcement due to radiation emitted within the volume $\mathcal{I}^{eq}_\nu(\vec{x}_1)$ and attenuated along the path ; (*right*) Reinforcement due to a contribution scattered from a direction $\vec{\omega}_1$ at a location $\vec{x}_1$.

$$\begin{aligned}\mathcal{I}_\nu(\vec{x}_0,\vec{\omega}_0) = \int_0^{+\infty} & dl_1\beta_\nu e^{-\beta_\nu l_1}\mathcal{H}(\vec{x}_1\in\partial\mathcal{D}_{\text{left}})\,\mathcal{I}^{\text{eq}}_{\nu,\text{left}} \\ &+ \mathcal{H}(\vec{x}_1\in\mathcal{D})k_{a,\nu}\mathcal{I}^{\text{eq}}_\nu(T(\vec{x}_1))dl_1e^{-\beta_\nu l_1} \\ &+ \mathcal{H}(\vec{x}_1\in\mathcal{D})k_{s,\nu}\left(\int_{4\pi}\mathrm{P}_{sca,\nu}(\vec{\omega}_1,\vec{\omega}_0)\mathcal{I}_\nu(\vec{x}_1,\vec{\omega}_1)\right)dl_1e^{-\beta_\nu l_1}\end{aligned} \tag{29}$$

The aforementioned equation can be given a statistical interpretation by incorporating probabilities (highlighted in blue) through the multiplication and division by the extinction spectral coefficient β_ν [11], as follows:

$$\begin{aligned}\mathcal{I}_\nu(\vec{x}_0,\vec{\omega}_0) = \int_0^{+\infty} & dl_1\beta_\nu e^{-\beta_\nu l_1}\mathcal{H}(\vec{x}_1\in\partial\mathcal{D}_{\text{left}})\,\mathcal{I}^{\text{eq}}_{\nu,\text{left}} \\ &+ \mathcal{H}(\vec{x}_1\in\mathcal{D})\frac{k_{a,\nu}}{\beta_\nu}\mathcal{I}^{\text{eq}}_\nu(T(\vec{x}_1))dl_1\beta_\nu e^{-\beta_\nu l_1} \\ &+ \mathcal{H}(\vec{x}_1\in\mathcal{D})\frac{k_{s,\nu}}{\beta_\nu}\left(\int_{4\pi}\mathrm{P}_{sca,\nu}(\vec{\omega}_1,\vec{\omega}_0)\mathcal{I}_\nu(\vec{x}_1,\vec{\omega}_1)\right)dl_1\beta_\nu e^{-\beta_\nu l_1}\end{aligned} \tag{30}$$

$\mathcal{I}_\nu(\vec{x}_0,\vec{\omega}_0)$ is hence expressed as the expectation of a random variable. In order to obtain a sample of this random variable, the optical paths are sampled backward starting from the initial position $\vec{x}_0$ and following the direction $\vec{\omega}_0$. The sampling process continues until the path intersects with either an emission location within the volume (as described by the second term of Eq. (30) and center picture in Fig. 13) or an emission location at the left boundary (as described in the first term of Eq. (30) and depicted in the left picture of Fig. 13). This is the principle of a *reverse* Monte Carlo algorithm to estimate $\mathcal{I}_\nu(\vec{x}_0,\vec{\omega}_0)$. [16].

In the context of a scattering event (as indicated by the third term of Eq. (30) and the right picture of Fig. 13) the trajectory continues and the quantity $\mathcal{I}_\nu(\vec{x}_1,\vec{\omega}_1)$ can also be represented as the expected value of a stochastic variable. This recursive term can be developed similarly to Eq. (30), for $j \geq 1$ may be expressed as:

$$\begin{aligned}\mathcal{I}_\nu(\vec{x}_j,\vec{\omega}_j) = \int_0^{+\infty} & dl_{j+1}\beta_\nu e^{-\beta_\nu l_{j+1}}\mathcal{H}(\vec{x}_{j+1}\in\partial\mathcal{D}_{\text{left}})\,\mathcal{I}^{\text{eq}}_{\nu,\text{left}} \\ &+ \mathcal{H}(\vec{x}_{j+1}\in\mathcal{D})\frac{k^\nu_a}{\beta_\nu}\mathcal{I}^{\text{eq}}_\nu(T(\vec{x}_{j+1}))dl_{j+1}\beta_\nu e^{-\beta_\nu l_{j+1}} \\ &+ \mathcal{H}(\vec{x}_{j+1}\in\mathcal{D})\frac{k^\nu_s}{\beta_\nu}\left(\int_{4\pi}\mathrm{P}_{sca,\nu}(\vec{\omega}_{j+1},\vec{\omega}_j)\mathcal{I}_\nu(\vec{x}_{j+1},\vec{\omega}_{j+1})\right)dl_{j+1}\beta_\nu e^{-\beta_\nu l_{j+}}\end{aligned} \tag{31}$$

The spectral radiative intensity can be mathematically represented as the expected value of the spectrum blackbody radiative intensity at the specific site where photon emission occurs.

$$\mathcal{I}_\nu(\vec{x}_0,\vec{\omega}_0) = \mathbb{E}(\mathcal{I}^{\text{eq}}_\nu(\vec{X}_{\text{end}})) \tag{32}$$

Where $\vec{X}_{\text{end}}$ is the random variable associated to the emission location at the end of the path.

B. Examples of optical paths sampled with the Monte Carlo algorithm

Two examples of typical Monte Carlo path are given in Figs. 14 and 15. On the first path example (see Fig. 14), the path starts at the location $\vec{x}_{\text{start}}$ in the j^{th} radiative

[7] Details are not given here, a more comprehensive understanding, please refer to the Chap 2. Sec 1.3. of Y. Maanane's thesis [26].

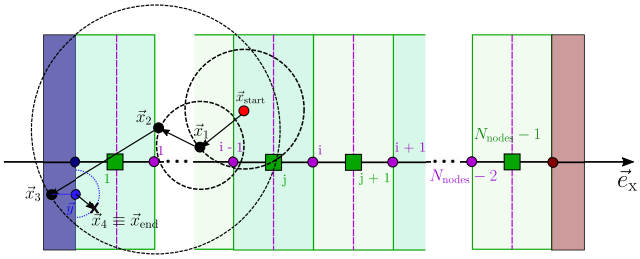

Figure 14: First example of a random path within the plate according to the algorithm represented in Fig. 4.

	$t_{e,FEMC}$ (s)	$t_{u,FEMC}$ (s)	t_{MC} (s)	$\frac{t_{MC}}{t_{FEMC}}$ (-)
1 + 1	6.209		1.308×10^2	21.06
2	∞	3.7×10^{-2}	2.504×10^2	6.749×10^3
3 + 3	6.253		2.705×10^2	43.25
4	∞	6.3×10^{-2}	4.57×10^2	7.278×10^3
7 + 7	6.194		38.65	6.240
8	∞	04.5×10^{-2}	2.221×10^2	4.987×10^3

Table 1
Computation times for the pure absorbing case with black walls (see Fig. 10).

mesh element (0), with $j_{start} = j$. Then a direction $\vec{\omega}$, a frequency ν and an extinction length l are sampled and the current position is set at a location $\vec{x}_1 \leftarrow \vec{x}_{start} + l_1 \vec{\omega}_1$ (1). The current position $\vec{x}_1$ is still in the volume $\mathcal{D}$ (2) and a scattering event occurs in this position (3). Hence, the path goes on, new direction and extinction length are sampled (1) and as previously, the path moves on to the next location $\vec{x}_2 \leftarrow \vec{x}_1 + l_2 \vec{\omega}_2$ within the volume $\mathcal{D}$ (2). Once again a scattering event occurs (3) and the path still goes on (1). This time, after sampling new direction and extinction length (1) and moving to the location $\vec{x}_3 \leftarrow \vec{x}_2 + l_3 \vec{\omega}_3$, the path meets the left boundary (2 then 3). A reflection event occurs at the location $\vec{y}$, hence a direction is sampled uniformly on the hemisphere and the path goes on to the location $\vec{x}_4 \leftarrow \vec{y} + ||\vec{y} - \vec{x}_3|| \vec{\omega}_4$ (4_a then 5_a). Eventually the path stops at the location $\vec{x}_{end} \equiv \vec{x}_4$, absorbed in the medium. The final index j_{end} is set equal to the index 1 of the first radiative mesh element, where the path has been absorbed. The corresponding Monte Carlo weight is equal to $w_k = 4\pi k_{a,\nu} \delta_x \left(\mathcal{I}_\nu^{eq}(j) - \mathcal{I}_\nu^{eq}(1) \right)$ with $\mathcal{I}_\nu^{eq}(1)$ depending on T_1 and computed with Eq. (5) (T_1 being the mean temperature of the first mesh radiative element).

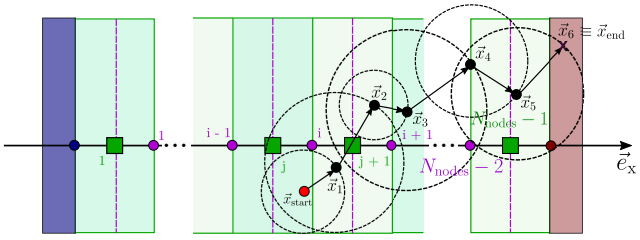

Figure 15: Second example of a random path within the plate according to the algorithm represented in Fig. 4.

On the second path example (see Fig. 15), the path starts at the same location $\vec{x}_{start}$ in the j^{th} radiative mesh element (0), with $j_{start} = j$. Similarly to the first path, this path undergoes multiple scattering events within the volume $\mathcal{D}$ from $\vec{x}_1$ until $\vec{x}_5$. On the last scattering event, at the location $\vec{x}_6$, the path meets the right boundary (2 then 3). This time an absorption event occurs on the right wall and the path stops in $\vec{x}_{end} \equiv \vec{x}_6$ (4_b). The final index j_{end} is set equal to the index N_{nodes} of the right wall radiative mesh element, where the path has been absorbed. The corresponding Monte Carlo weight is equal to $w_k = 4\pi k_{a,\nu} \delta_x \left(\mathcal{I}_\nu^{eq}(j) - \mathcal{I}_\nu^{eq}(N_{nodes}) \right)$ with $\mathcal{I}_\nu^{eq}(N_{nodes})$ depending on T_{right} and computed with Eq. (5).

C. Computation times

All of the computation times regarding the finite differences–Monte Carlo algorithm and the finite differences–Monte Carlo algorithm are summarized in Tabs. 1 to 3. Each of the following computation time is given for a laptop with an Intel Core i5 - CPU @ 1.60GHz × 8, RAM : 16Gb.

The computation time needed to estimate the functions with the finite differences–functional Monte Carlo algorithm are noted $t_{e,FEMC}$, the computation time needed to use the functions to estimate the temperature profile with the finite differences–functional Monte Carlo algorithm are noted $t_{u,FEMC}$, the computation time needed to estimate the temperature profiles with the finite differences–Monte Carlo algorithm are noted t_{MC}. A time gain, noted $\frac{t_{MC}}{t_{FEMC}}$, is the ratio of the time t_{MC} needed to estimate the temperature profile with the finite differences–Monte Carlo algorithm and the time t_{FEMC} needed to estimate the temperature profile with the finite differences–functional Monte Carlo algorithm. The time t_{FEMC} is either equal to $t_{e,FEMC} + t_{u,FEMC}$ if the function is computed for the first time and is used right after or only equal to $t_{u,FEMC}$ if the function has already been calculated and needs to be used to estimate the profile.

For the sake of clarity, the time computations are referenced with numbers corresponding to the previous cases scheme in Fig. 10. The computation times are divided in the three corresponding studied case from Viskanta et al.: times presented in Tab. 1 stand for the pure absorbing medium with black walls [46], those presented in Tab. 2 stand for the same pure absorbing medium with grey walls [45] (see Sec. 3.1 and Sec. 3.2) and the times presented in Tab. 3 are for the absorbing and scattering medium with black walls [44] (see Sec. 3.3).

In average and for each of the three configuration studied, the computation time needed to estimate and use the functions is around 6 s, as indicated for the functions 1 , 3 and 7 in Tab. 1, functions 1 (calculated only once in the first configuration), 9 and 10 in Tab. 2 and functions

	$t_{e,FEMC}$ (s)	$t_{u,FEMC}$ (s)	t_{MC} (s)	$\frac{t_{MC}}{t_{FEMC}}$ (-)
1 + 1	6.209		1.308×10^2	21.06
9 + 9	6.040		1.216×10^2	20.13
10 + 10	3.064		1.503×10^2	49.04

Table 2
Computation times for the pure absorbing case with grey walls (see Fig. 10).

	$t_{e,FEMC}$ (s)	$t_{u,FEMC}$ (s)	t_{MC} (s)	$\frac{t_{MC}}{t_{FEMC}}$ (-)
3 + 5	6.253		2.705×10^2	43.25
6	∞	6.3×10^{-2}	4.57×10^2	7.278×10^3
11 + 11	7.048		2.39×10^2	33.9
12	∞	3.83×10^{-2}	5.842×10^2	1.526×10^4
13 + 13	3.222		4.18×10^{-1}	1.3×10^{-1}
14	∞	2×10^{-3}	3.89×10^{-1}	1.736×10^2

Table 3
Computation times for the absorbing and scattering case with black walls (see Fig. 10).

3 (calculated only once, as well, in the first configuration), 11 and 13 in Tab. 3.

The computation time needed to use the function to calculate the temperature profiles, whatever the case studied, in always lower than a second. The computation time needed to estimate the temperature profile with the MC/FD method is in the order of magnitude of 10^2 seconds, in average. There is an exception for the last cases 13 and 14 in which the medium is perfectly non absorbing and purely scattering.

Regarding the time ratio, if the functions need to be estimated with finite differences–functional Monte Carlo algorithm the time gain of the latter algorithm compared to the finite differences–Monte Carlo algorithm varies from around 20, in the case of the pure absorbing medium case with the black walls until around 40 in the other cases. If the functions only need to be used, the time gain of the finite differences–functional Monte Carlo algorithm compared to the finite differences–Monte Carlo one varies from an order of magnitude of 10^2 to 10^3.

References

[1] Asllanaj, F., Parent, G., Jeandel, G., 2007. Transient radiation and conduction heat transfer in a gray absorbing-emitting medium applied on two-dimensional complex-shaped domains. Numerical Heat Transfer, Part B: Fundamentals 52, 179–200. doi:10.1080/10407790701227351.

[2] Chen, X., Sun, C., Xia, X., Liu, R., Wang, F., a. Conjugated heat transfer analysis of a foam filled double-pipe heat exchanger for high-temperature application. International Journal of Heat and Mass Transfer 134, 1003–1013. doi:10.1016/j.ijheatmasstransfer.2019.01.100.

[3] Chen, X., Wang, F., Yan, X., Cheng, Z., Han, Y., Jie, Z., b. Thermal and chemical analysis of methane dry reforming in a volumetric reactor under highly concentrated solar radiation. Solar Energy 162, 187–195. doi:10.1016/j.solener.2018.01.032.

[4] Chen, X., Wang, F., Yan, X., Han, Y., Cheng, Z., Jie, Z., c. Thermo-chemical performance of solar driven CO2 reforming of methane in volumetric reactor with gradual foam structure. Energy 151, 545–555. doi:10.1016/j.energy.2018.03.086.

[5] Dauchet, J., Bezian, J.J., Blanco, S., Caliot, C., Charon, J., Coustet, C., El Hafi, M., Eymet, V., Farges, O., Forest, V., Fournier, R., Galtier, M., Gautrais, J., Khuong, A., Pelissier, L., Piaud, B., Roger, M., Terrée, G., Weitz, S., . Addressing nonlinearities in monte carlo. Scientific Reports 8, 13302. doi:10.1038/s41598-018-31574-4.

[6] Dunn, W., 1981. Inverse Monte Carlo analysis. Journal of Computational Physics 41, 154–166. doi:10.1016/0021-9991(81)90085-1.

[7] Dunn, W., Shultis, J., 2009. Monte Carlo methods for design and analysis of radiation detectors. Radiation Physics and Chemistry 78, 852–858. doi:10.1016/j.radphyschem.2009.04.030.

[8] Eymet, V., Fournier, R., Dufresne, J.L., Lebonnois, S., Hourdin, F., Bullock, M.A., a. Net exchange parameterization of thermal infrared radiative transfer in venus' atmosphere. Journal of Geophysical Research 114, E11008. doi:10.1029/2008JE003276.

[9] Eymet, V., Poitou, D., Galtier, M., El Hafi, M., Terrée, G., Fournier, R., b. Null-collision meshless monte-carlo—application to the validation of fast radiative transfer solvers embedded in combustion simulators. Journal of Quantitative Spectroscopy and Radiative Transfer 129, 145–157. doi:10.1016/j.jqsrt.2013.06.004.

[10] Farges, O., Penazzi, L., 2024. 1D conduction radiation coupled heat transfer in an absorbing medium : Monte Carlo functionnal modeling. URL: https://doi.org/10.57745/MPSCI4, doi:10.57745/MPSCI4.

[11] Galtier, M., . Approche statistique du rayonnement dans les milieux gazeux hétérogènes : de l'échantillonnage des transitions moléculaires au calcul de grandeurs radiatives. phdthesis. Ecole des Mines d'Albi-Carmaux.

[12] Galtier, M., Blanco, S., Caliot, C., Coustet, C., Dauchet, J., El Hafi, M., Eymet, V., Fournier, R., Gautrais, J., Khuong, A., Piaud, B., Terrée, G., . Integral formulation of null-collision monte carlo algorithms. Journal of Quantitative Spectroscopy and Radiative Transfer 125, 57–68. doi:10.1016/j.jqsrt.2013.04.001.

[13] Galtier, M., Roger, M., André, F., Delmas, A., 2017. A symbolic approach for the identification of radiative properties. Journal of Quantitative Spectroscopy and Radiative Transfer 196, 130–141. doi:10.1016/j.jqsrt.2017.03.026.

[14] Hottel, H.C., . Radiant Heat Transmission. 3rd edition ed., McGraw-Hill.

[15] Howell, J., Mengüc, M., Daun, K., Siegel, R., 2020. Thermal Radiation Heat Transfer (7th ed.). CRC Press. doi:https://doi.org/10.1201/9780429327308.

[16] Howell, J.R., Daun, K.J., . The past and future of the monte carlo method in thermal radiation transfer. Journal of Heat Transfer 143, 100801. doi:10.1115/1.4050719.

[17] Howell, J.R., Menguc, M.P., Siegel, R., . Thermal Radiation Heat Transfer. 0 ed., CRC Press. doi:10.1201/9781439894552.

[18] Howell, J.R., Mengüç, M.P., . Radiative transfer configuration factor catalog: A listing of relations for common geometries. Journal of Quantitative Spectroscopy and Radiative Transfer 112, 910–912. doi:10.1016/j.jqsrt.2010.10.002.

[19] Jannot, Y., Degiovanni, A., 2018. Thermal Properties Measurement of Materials. Wiley-ISTE.

[20] Jannot, Y., Degiovanni, A., 2019. An improved model for the parallel hot wire: Application to thermal conductivity measurement of low density insulating materials at high temperature. International Journal of Thermal Sciences 142, 379–391. doi:https://doi.org/10.1016/j.ijthermalsci.2019.04.026.

[21] Jannot, Y., Degiovanni, A., Schick, V., Meulemans, J., 2020. Thermal diffusivity measurement of insulating materials at high temperature with a four-layer (4l) method. International Journal of Thermal Sciences 150, 106230. doi:https://doi.org/10.1016/j.ijthermalsci.2019.106230.

[22] Li, Z.H., Li, X.L., Xia, X.L., Sun, C., . A hybrid strategy for solving radiation-conduction in irregular geometries filled with gray semitransparent medium using monte carlo method combined with blocked-off and embedded boundary treatments. Numerical Heat Transfer, Part B: Fundamentals 77, 22–41. doi:10.1080/10407790.2019.1690368.

[23] Liu, L., Xu, X., . Monte carlo ray-tracing simulation for radiative heat transfer in turbulent fluctuating media under the optically thin fluctuation approximation. Journal of Quantitative Spectroscopy and Radiative Transfer 84, 349–355. doi:10.1016/S0022-4073(03)00185-7.

[24] Low, Z., Baillis, D., 2021. Radiative behavior of low-porosity ceramics: I-development and applications of a physical optics modeling approach. Journal of Quantitative Spectroscopy and Radiative Transfer 272, 107819. doi:https://doi.org/10.1016/j.jqsrt.2021.107819.

[25] Low, Z., Novikov, A., De Sousa Meneses, D., Baillis, D., 2021. Radiative behavior of low-porosity ceramics: Ii–experimental and numerical study of porous alumina up to high temperatures. Journal of Quantitative Spectroscopy and Radiative Transfer 272, 107821. doi:https://doi.org/10.1016/j.jqsrt.2021.107821.

[26] Maanane, Y., . Identification expérimentale de propriétés radiatives à partir de méthodes Monte Carlo Symbolique : application à des matériaux hétérogènes à haute température. phdthesis. INSA Lyon.

[27] Maanane, Y., Roger, M., Delmas, A., Galtier, M., André, F., 2020. Symbolic monte carlo method applied to the identification of radiative properties of a heterogeneous material. Journal of Quantitative Spectroscopy and Radiative Transfer 249, 107019. URL: https://www.sciencedirect.com/science/article/pii/S0022407319307964, doi:https://doi.org/10.1016/j.jqsrt.2020.107019.

[28] Machin, G., Anhalt, K., Battuello, M., Bourson, F., Dekker, P., Diril, A., Edler, F., Elliott, C., Girard, F., Greenen, A., Kňazovická, L., Lowe, D., Pavlásek, P., Pearce, J., Sadli, M., Strnad, R., Seifert, M., Vuelban, E., 2016. The european project on high temperature measurement solutions in industry (hitems) – a summary of achievements. Measurement 78, 168–179. doi:https://doi.org/10.1016/j.measurement.2015.09.033.

[29] Méso-Star, 2023. Star–engine. URL: https://www.meso-star.com/projects/star-engine/star-engine.html.

[30] Modest, M.F., . Radiative Heat Transfer. Third edition ed., Academic Press. doi:https://doi.org/10.1016/C2010-0-65874-3.

[31] Niederer, M., Strommer, S., Steinboeck, A., Kugi, A., . A simple control-oriented model of an indirect-fired strip annealing furnace. International Journal of Heat and Mass Transfer 78, 557–570. doi:10.1016/j.ijheatmasstransfer.2014.06.080.

[32] Ouchtout, S., Rousseau, B., Favennec, Y., 2022. Finite element framework for modeling conducto-radiative transfers within heterogeneous media at both discrete and continuous scales. International Journal of Heat and Mass Transfer 197, 123274. doi:https://doi.org/10.1016/j.ijheatmasstransfer.2022.123274.

[33] Penazzi, L., Blanco, S., Caliot, C., Coustet, C., El Hafi, M., Fournier, R., Gautrais, J., Golijanek-Jędrzejczyk, A., Sans, M., . Path integrals formulations leading to propagator evaluation for coupled linear physics in large geometric models. Computer Physics Communications Journal 294. doi:https://doi.org/10.1016/j.cpc.2023.108911.

[34] Penazzi, L., Blanco, S., Caliot, C., Coustet, C., El-Hafi, M., Fournier, R.A., Gautrais, J., Sans, M., 2021. Transfer function estimation with SMC method for combined heat transfer: insensitivity to detail refinement of complex geometries, in: CHT-21 ICHMT - International Symposium on Advances in Computational Heat Transfer, Rio de Janeiro (online), Brazil. pp. 383–386. URL: https://imt-mines-albi.hal.science/hal-03374353.

[35] Penazzi, L., Blanco, S., Caliot, C., Coustet, C., Hafi, M.E., Fournier, R., M. Galtier, L.I., Roger, M., 2019. Toward the use of Symbolic Monte Carlo for conduction-convection-radiation coupling in complex geometries, in: Proceeding of Proceedings of the 9th International Symposium on Radiative Transfer, RAD-19, Begellhouse. pp. 311–318. doi:10.1615/RAD-19.380.

[36] Penazzi, L., Farges, O., 2022. star-CoRad. URL: https://hal.science/hal-03798046.

[37] Penazzi, L., Jannot, Y., Meulemans, J., Farges, O., Schick, V., 2022. Influence of radiation heat transfer on parallel hot-wire thermal conductivity measurements of semi-transparent materials at high temperature. International Journal of Thermal Sciences 179, 107690. doi:https://doi.org/10.1016/j.ijthermalsci.2022.107690.

[38] Perraudin, D.Y., Haussener, S., 2017. Numerical quantification of coupling effects for radiation-conduction heat transfer in participating macroporous media: Investigation of a model geometry. International Journal of Heat and Mass Transfer 112, 387–400. doi:https://doi.org/10.1016/j.ijheatmasstransfer.2017.03.079.

[39] Royer, A., Farges, O., Boulet, P., Burot, D., . A new method for modeling radiative heat transfer based on bayesian artificial neural networks and monte carlo method in participating media. International Journal of Heat and Mass Transfer 201, 123610. doi:10.1016/j.ijheatmasstransfer.2022.123610.

[40] Ruan, L., Qi, H., Liu, L., Tan, H., . The radiative transfer in cylindrical medium and partition allocation method by overlap regions. Journal of Quantitative Spectroscopy and Radiative Transfer 86, 343–352. doi:10.1016/j.jqsrt.2003.08.011.

[41] Sans, M., Schick, V., Parent, G., Farges, O., 2020. Experimental characterization of the coupled conductive and radiative heat transfer in ceramic foams with a flash method at high temperature. International Journal of Heat and Mass Transfer 148, 119077. doi:https://doi.org/10.1016/j.ijheatmasstransfer.2019.119077.

[42] Shuai, Y., Zhang, H.C., Tan, H.P., . Radiation symmetry test and uncertainty analysis of monte carlo method based on radiative exchange factor. Journal of Quantitative Spectroscopy and Radiative Transfer 109, 1281–1296. doi:10.1016/j.jqsrt.2007.10.001.

[43] Université de Lorraine, 2023. Méso–centre explor. URL: https://explor.univ-lorraine.fr/.

[44] Viskanta, R., 1965. Heat Transfer by Conduction and Radiation in Absorbing and Scattering Materials. Journal of Heat Transfer 87, 143–150. doi:10.1115/1.3689035.

[45] Viskanta, R., Grosh, R.J., 1962a. Effect of surface emissivity on heat transfer by simultaneous conduction and radiation. International Journal of Heat and Mass Transfer 5, 729–734. doi:https://doi.org/10.1016/0017-9310(62)90203-X.

[46] Viskanta, R., Grosh, R.J., 1962b. Heat Transfer by Simultaneous Conduction and Radiation in an Absorbing Medium. Journal of Heat Transfer 84, 63–72. doi:10.1115/1.3684294.

[47] Yang, W.J., Taniguchi, H., Kudo, K., . Radiative Heat Transfer by the Monte Carlo Method. volume 27 of *Advances in heat transfer*. Academic Press.

[48] Zarrouati, M., Enguehard, F., Taine, J., . Radiative transfer within strongly non homogeneous porous media: Application to a slab of packed particles. International Journal of Heat and Mass Transfer 91, 936–947. doi:10.1016/j.ijheatmasstransfer.2015.08.024.

[49] Zhang, Y., Gicquel, O., Taine, J., . Optimized emission-based reciprocity monte carlo method to speed up computation in complex systems. International Journal of Heat and Mass Transfer 55, 8172–8177. doi:10.1016/j.ijheatmasstransfer.2012.05.028.

[50] Zier, M., Stenzel, P., Kotzur, L., Stolten, D., 2021. A review of decarbonization options for the glass industry. Energy Conversion and Management: X 10, 100083. doi:https://doi.org/10.1016/j.ecmx.2021.100083.